ANALYSIS OF MINIATURIZED, CIRCULARLY POLARIZED ANTENNAS

FOR BIDIRECTIONAL PROPAGATION

by

MASON C. MOORE

(Under the Direction of Sungkyun Lim)

ABSTRACT

Size reduction is necessary to fit the recent demand for small sized communication systems in consumer electronics. Wireless communication systems rely on antennas for long range transmission of signals, so size reduced antennas have been sought after in recent years. Also, not many antennas are designed for use in bidirectional scenarios like subways, tunnels, bridges, etc. Three sized reduced antennas with circular polarization are presented for use in bidirectional communication systems. An electrically small pattern reconfigurable array, an electrically small two-sided printed cross dipole, and a size reduced printed wideband antenna are introduced within this thesis. All antennas' results are obtained from simulation, with two of the antenna designs being measured to verify their results.

INDEX WORDS: Electrically small antennas, Reconfigurable arrays, Circular polarization, Bidirectional antennas.

ANALYSIS OF SIZE-REDUCED, CIRCULARLY POLARIZED ANTENNAS FOR BIDIRECTIONAL PROPAGATION

by

MASON C. MOORE

B.S., Georgia Southern University, 2019

M.S., Georgia Southern University, 2021

A Thesis Submitted to the Graduate Faculty of Georgia Southern University in Partial Fulfillment of the Requirements for the Degree

MASTER OF SCIENCE

ANALYSIS OF MINIATURIZED, CIRCULARLY POLARIZED ANTENNAS

FOR BIDIRECTIONAL PROPAGATION

by

MASON C. MOORE

Major Professor:	Sungkyun Lim
Committee:	Mohammad Ahad
	Fernando Rios

Electronic Version Approved:
July 2021

DEDICATION

First and most importantly, I would like to thank my loving parents, sister, girlfriend, and friends who have pushed me to get to this point. Without their love and support this would not have been possible.

ACKNOWLEDGMENTS

I would like to thank Dr. Sungkyun Lim for his supervision and dedication to my education. Also, I would like to thank my committee members Dr. Ahad and Dr. Rios for taking time to review my thesis. Additionally, I would like to thank my peers in the Antennas and Wireless Propagation laboratory, Kevin Leon, John Verboom, and Grant Evans for their advice and help with my research.

TABLE OF CONTENTS

Page

LIST OF TABLES

Page

LIST OF FIGURES

Page

CHAPTER 1

INTRODUCTION

1.1 Background of Antenna Characteristics

Antennas play an important role in the digital age as they are capable of sending electro-magnetic (EM) waves over vast distances with no physical connection. Applications are broad but not limited to RFID, satellite, wireless power transfer, cellular phones, and radio. All EM waves travel at the same speed (c) which is the speed of light, so two of the most important attributes are communicated through wavelength (λ) and frequency (f). The relationship between these characteristics is shown in Equation 1 below.

$$c = \lambda * f$$

Equation 1. Speed of Light [1]

The most basic antenna design is the λ/2 dipole. This configuration consists of two λ/4 wires orientated end to end and connected in the middle by a feed. In most cases, the feed is a coaxial cable with the inner conductor connected to one arm and the outer conductor connected to the other arm. For many antenna designs, the goal is to match it to the characteristic impedance of the transmission line, which is 50 Ω. How well an antenna is matched to the characteristic impedance is translated through the reflection coefficient (Γ), which is the relationship between the impedance load (Z_L) and the source impedance (Z_0) seen in Equation 2. In a majority of instances, the reflection coefficient is converted into the return loss which is the common output for antenna measurement systems like a network analyzer.

$$\Gamma = \frac{Z_L - Z_0}{Z_L + Z_0}$$

Equation 2. Reflection Coefficient [1]

$$S_{11}(dB) = -20 * \log_{10}(\Gamma)$$

Equation 3. Return Loss [1]

Antennas have an operating frequency range that is called their impedance bandwidth, which is traditionally the frequency range at which their S_{11} is less than -10 dB. At -10 dB, the antenna transmits 90% and reflects 10% of the power provided by the transmission line. The previously shown λ/2 dipole has

a fractional bandwidth of nearly 10%, but having a S_{11} below -10 dB does not mean the antenna will radiate a signal at a given frequency. Far-field parameters such as directivity, gain, and realized gain pertain to the measurement of how well an antenna propagates in a given direction. The equations for directivity, gain, and realized gain are shown in Equation 4, 5, and 6 below.

$$D(\theta,\varphi) = \frac{Power\ Density(\theta,\varphi)}{Total\ Radiated\ Power/4\pi}$$

Equation 4. Directivity [1]

$$G(\theta,\varphi) = \eta_r * D(\theta,\varphi)$$

Equation 5. Gain [1]

$$RG(\theta,\varphi) = (1-\Gamma^2) * G(\theta,\varphi)$$

Equation 6. Realized Gain [1]

Realized gain is the most common metric for antenna parameters as it considers efficiency (η_r) and mismatching loss. In most cases, the realized gain is presented in a logarithmic scale and in dBi (with respect to an isotropic radiator).

1.2 Antenna Polarization

Antennas can have three different polarizations (linear, circular, and elliptical) based upon the direction of the electric field vector. Linear polarization (LP) occurs when the electric field vector is contained in a single plane such as the propagation from a λ/2 dipole. The two most common senses for LP are vertical and horizontal, which correspond to the electric field vector direction with respect to the earth. Antennas are classified as having circular polarization when the electric field vector rotates while propagating in a certain direction. Just as LP has vertical and horizontal senses, circular polarization has right-handed (RHCP) and left-handed (LHCP) depending on the counterclockwise and clockwise rotation of the electric field vector, respectively. The classification for polarization depends on the ratio between the magnitude of electric field vector axes. This ratio is known as the axial ratio which is shown in Equation 7.

$$Axial\ Ratio = \frac{Major\ Axis}{Minor\ Axis}$$

Equation 7. Axial Ratio [1]

A linear axial ratio value of infinity corresponds to LP and a linear axial ratio value of 1 corresponds to circular polarization, any number in between is classified as elliptically polarized. Generally, axial ratio is presented in a logarithmic scale with a value between 0 and 3 dB corresponding to circular polarization.

Polarization mismatch can occur when two antennas (one transmitting and one receiving) have different polarizations. For example, a vertically polarized antenna receiving a signal from a horizontally polarized antenna will have severely reduced received power. Similarly, circularly polarized antennas with opposite senses used in a communication system have less dramatic losses as shown with the Polarization Loss Factors (PLF) in Table 1.

	Receiver Antenna (PLF)			
Transmitter Antenna	Vertical LP	Horizontal LP	RHCP	LHCP
Vertical LP	1	0	½	½
Horizontal LP	0	1	½	½
RHCP	½	½	1	0
LHCP	½	½	0	1

Table 1. Polarization Loss Factor for polarization sense cases.

Since 3-dB axial ratio corresponds to circular polarization, in linear terms this is the magnitude of the major axis E-field vector being two times larger than the magnitude minor axis E-field vector. PLF is given in equation 8 below and relates the lost power to the angle between the transmitted, *pw*, and received, *pa*, electric field vectors [2].

$$Polarization\ Loss\ Factor\ (PLF) = |\widehat{pw} \bullet \widehat{pa}|^2$$

Equation 8. Polarization Loss Factor [2]

Circular polarization can be achieved with varying antennas design, but one of the easiest is a crossed dipole. Traditionally, two dipoles of the same length can be placed perpendicular to each other to produce circular polarization, but this requires two separate feeds which increases complexity of the system. The two separately fed dipoles require an external feeding network that is capable of shifting the input phase of

one of the dipoles by 90º. A single feed circularly polarized (CP) crossed dipole is shown in Figure 1, by having two perpendicularly orientated dipoles with different lengths. The shorter dipole is nearly 80% of the length of the longer dipole, which causes the real part of their admittance to be equal, but the angle of input admittances are different by 90º [3].

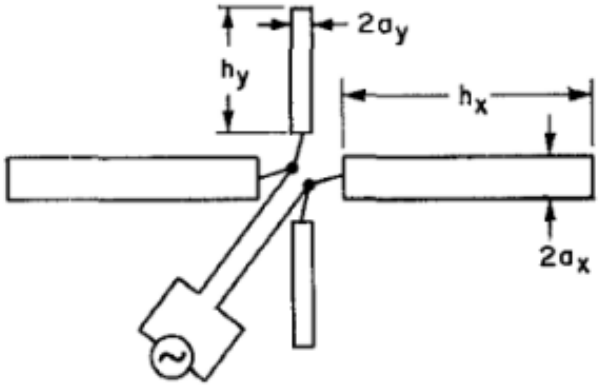

Figure 1. Crossed dipole [3].

Many other antenna designs are capable of generating circular polarization as long as the structure of the antenna can host the surface current characteristics that are observed from circular polarization. The magnitude and direction of the surface current is generally used as an explanation and justification of circular polarization. The surface current of circular polarization is shown in Figure 2. The cross dipole is shown at four phases with a 90ºshift between neighboring phases. The magnitude of the strong current magnitude stays consistent at each phase, but the direction of the current rotates in correspondence with the sense of circular polarization. Between 0ºand 90º the strong direction moves from left-to-right to bottom-to-top, which is a counterclockwise rotation of strong current direction. A clockwise rotation declares a LHCP propagation while a counterclockwise rotation is a RHCP propagation.

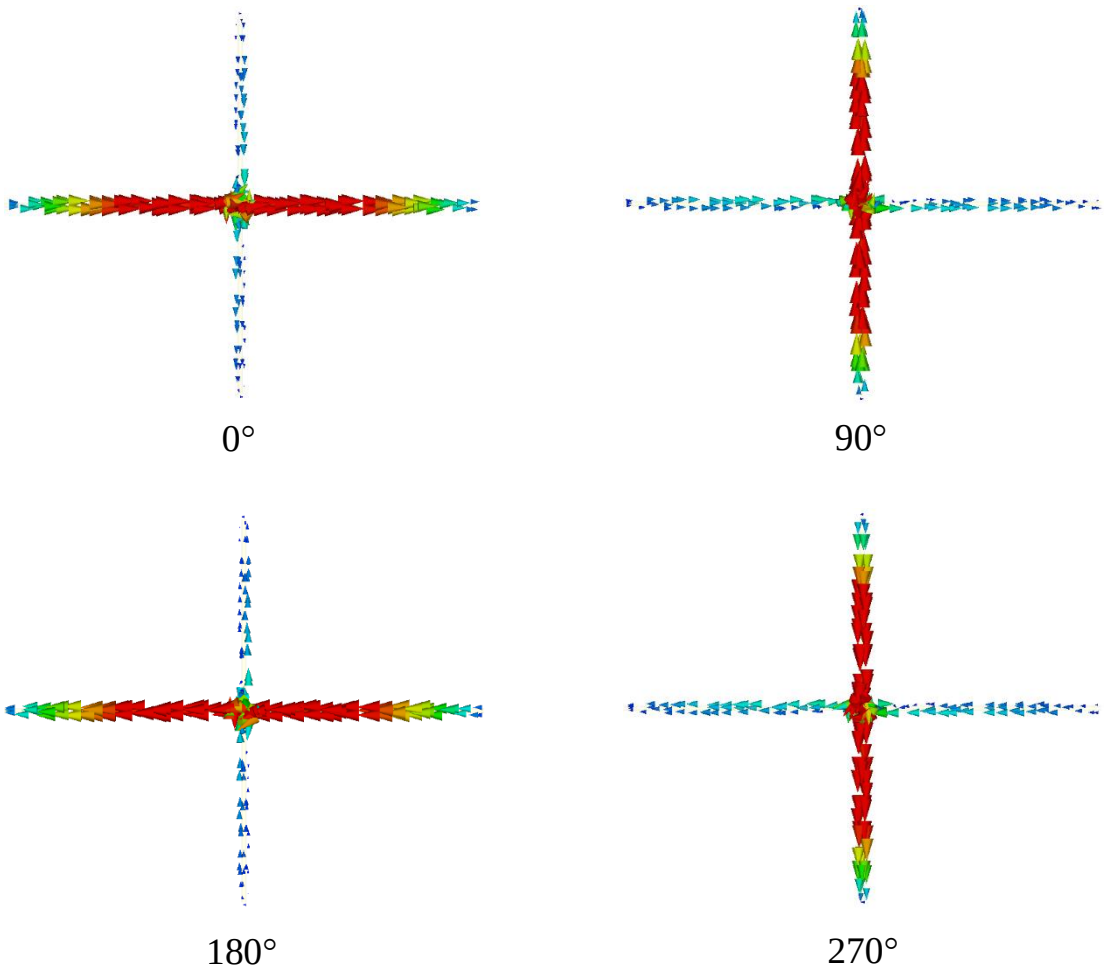

Figure 2. Surface current distribution for a circularly polarized antenna.

1.3 The Yagi-Uda Antenna

In 1926, the Yagi-Uda antenna was developed by Shintaro Uda. Known as the yagi antenna, the Yagi-uda is a dipole driven element with additional parasitic elements to increase directivity. Parasitic elements are named as such, as there is no physical connection to the driven element, thus the parasitic elements operate by being in close proximity to the driven element. The parasitic elements may be reflector or directors, but most commonly yagi antennas have one reflector and one or more directors as shown in Figure 3.

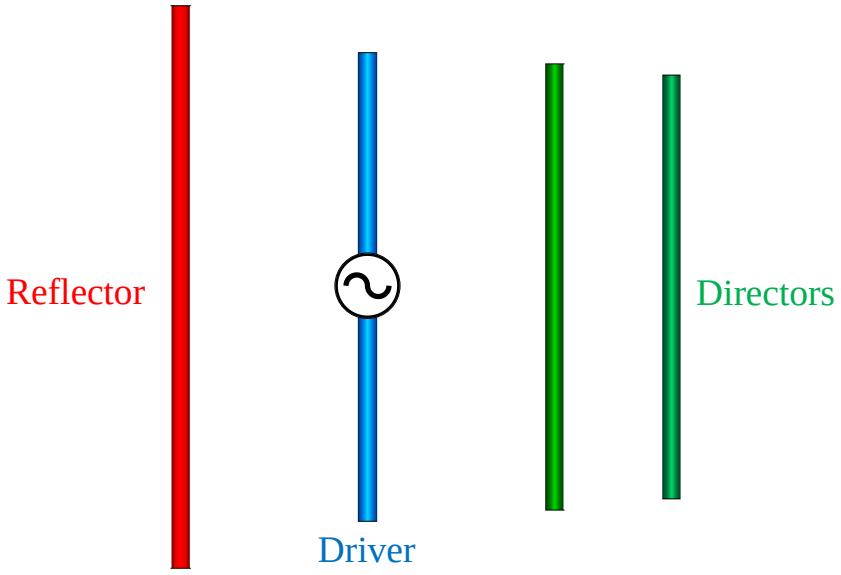

Figure 3. Traditional Yagi Configuration.

The yagi configuration produces a directive pattern towards the directors, with more directors providing a higher directivity. Simply adding a reflector and director to a dipole driver can increase the realized gain by 7 dB when compared to a standalone λ/2 dipole. However, additional directors begin to provide diminishing gains as shown in Table 2. The dimensions for the parasitic elements with multiple directors can also be seen in Table 2.

1.4 Electrical Size Reduction

Antenna dimensions are traditionally presented with respect to their resonant frequencies wavelength so that they can be repurposed and designed at different frequencies. Another metric that is commonly used is the electrical size or *kr*. It is calculated by multiplying the wave number, *k*, and the radius, *r*, of the smallest sphere capable of enclosing the whole antenna. The equation for wave number is shown in Equation 8. For a λ/2 dipole, the *kr* is nearly 1.6 which is considered an electrically large antenna as it has a *kr* greater than 1. In contrast, an electrically small antenna has a *kr* less than 1.

$$k = \frac{2\pi}{\lambda}$$

Equation 8. Wave number [1]

TABLE I. OPTIMIZED LENGTHS OF PARASITIC ELEMENTS
FOR YAGI ANTENNAS OF SIX DIFFERENT LENGTHS

		LENGTH OF YAGI IN WAVELENGTHS					
		0.4	0.8	1.20	2.2	3.2	4.2
LENGTH OF REFLECTOR, λ		0.482	0.482	0.482	0.482	0.482	0.475
LENGTH OF DIRECTOR, λ	1st	0.424	0.428	0.428	0.432	0.428	0.424
	2nd		0.424	0.420	0.415	0.420	0.424
	3rd		0.428	0.420	0.407	0.407	0.420
	4th			0.428	0.398	0.398	0.407
	5th				0.390	0.394	0.403
	6th				0.390	0.390	0.398
	7th				0.390	0.386	0.394
	8th				0.390	0.386	0.390
	9th				0.398	0.386	0.390
	10th				0.407	0.386	0.390
	11th					0.386	0.390
	12th					0.386	0.390
	13th					0.386	0.390
	14th					0.386	
	15th					0.386	
SPACING BETWEEN DIRECTORS, IN λ		0.20	0.20	0.25	0.20	0.20	0.308
GAIN RELATIVE TO HALF-WAVE DIPOLE IN dB		7.1	9.2	10.2	12.25	13.4	14.2
DESIGN CURVE (SEE FIG. 9)		(A)	(B)	(B)	(C)	(B)	(D)

ELEMENT DIAMETER = 0.0085
f = 400 MHz
REFLECTOR SPACED 0.2λ BEHIND DRIVEN ELEMENT

Table 2. Optimized for yagi antennas with different number of directors [4].

One of the most common techniques to reduce the electrical size of wire antennas is the use of top loading. This method utilizes bending the end of the elements to conform to a smaller radius and is shown in Figure 4. First, a standard λ/2 dipole is shown in Figure 4(a) with no top loading. Then, a top loaded

antenna is shown in Figure 4(b) with a 90º bend. Next, as shown in Figure 4(c) a top loaded λ/2 dipole is presented with top loading that follows the perimeter of the circle to further reduce the *kr*. Since the top loading follows the arc of a circle, it does not add any radius to the sphere enclosing the antenna as compared to the 90º bent top loading.

For multi-element arrays, size reduction by simply placing the elements closer together is possible but there is a limit. For example, a two-element yagi-uda antenna normally has a spacing between the driver and director of around 0.2λ, but spacing can be reduced to the magnitude of 0.02λ with reduced radiation resistance.

Reducing the size of an antenna is important as it saves space in applied systems, but there is a limit to how small *kr* can go before results start to diminish. The two antenna parameters that are decreased as antenna size is reduced below 0.8 *kr* are the impedance bandwidth and the radiation efficiency. The limitations on size reduction has been thoroughly studied and the theoretical limit for the bandwidth-efficiency product is shown in Figure 5. Thus, methods to counteract the lowered bandwidth and efficiency are implemented on antennas with a 0.8 *kr* or lower.

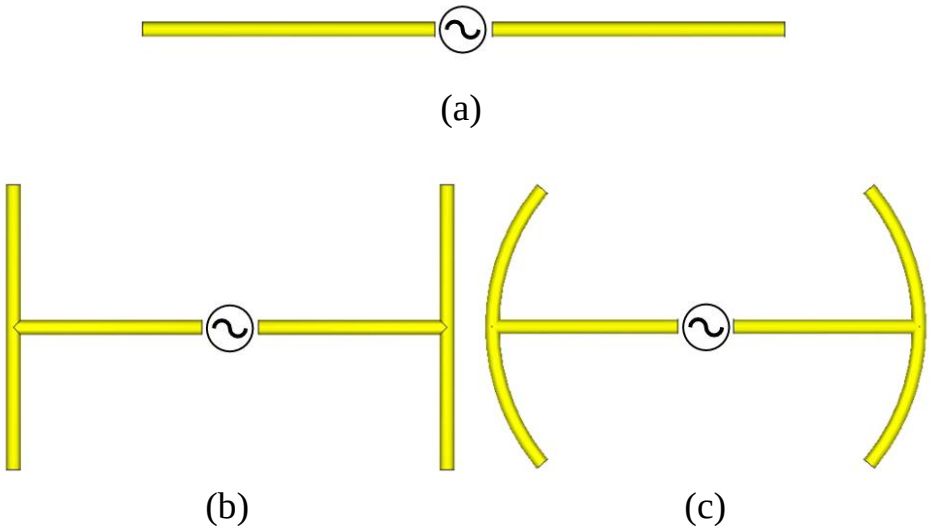

Figure 4. Top loading evolution. (a) No top loading, (b) 90º bend top loading, and (c) curved top loading.

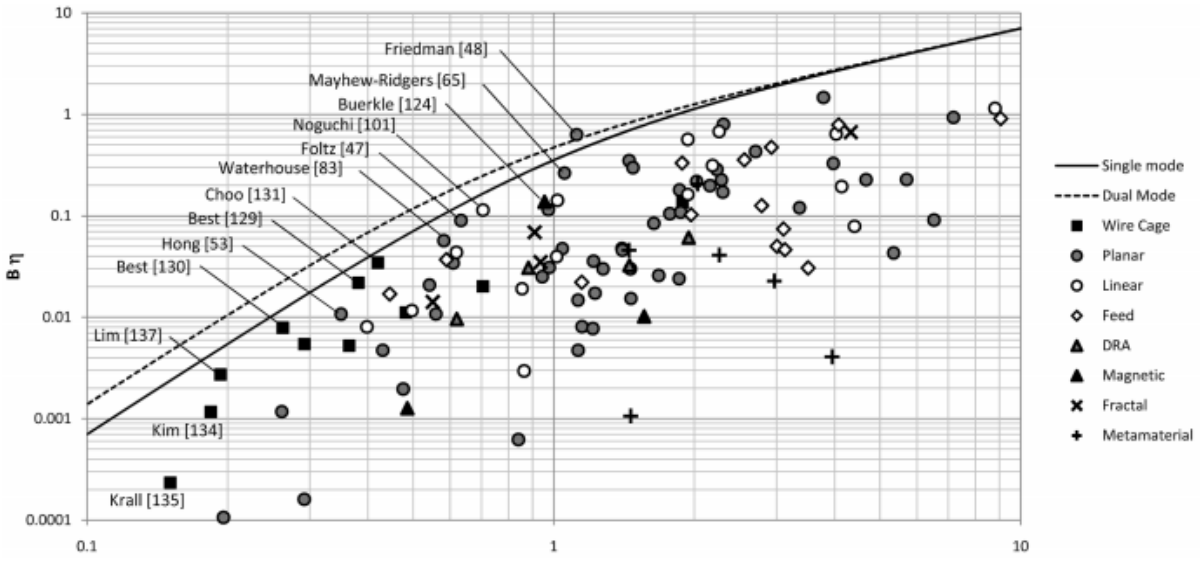

Figure 5. Theoretical limit of bandwidth-efficiency product versus *kr* [5].

As previously mentioned, most antennas are designed to match with the characteristic impedance of 50 Ω but reducing the electrical size and/or close element spacing causes a drop in radiation resistance and therefore the impedance bandwidth. Thus, several methods have been devised to boost the radiation resistance for proper matching. One technique to boost radiation resistance in electrically small antenna is using folds which can slightly increase the *kr* of the antenna. An example of folds is presented in Figure 6, which shows folds being utilized on a 0.84 *kr* two element parasitic array. Although the antenna's electrical size is not smaller than 0.8, the reduction in radiation resistance is caused from a close element spacing of 0.025λ. Subsequently, two folds are connected symmetrically on the driver to boost the radiation resistance for proper matching. Another approach to boost radiation resistance that does not affect the *kr* is the use of T-matching, which is commonly used in RFID tags. An RFID antenna with T-matching can be seen in Figure 7. Since the T-matching is placed in close proximity to the feed, it does not add any radius for the *kr* calculation.

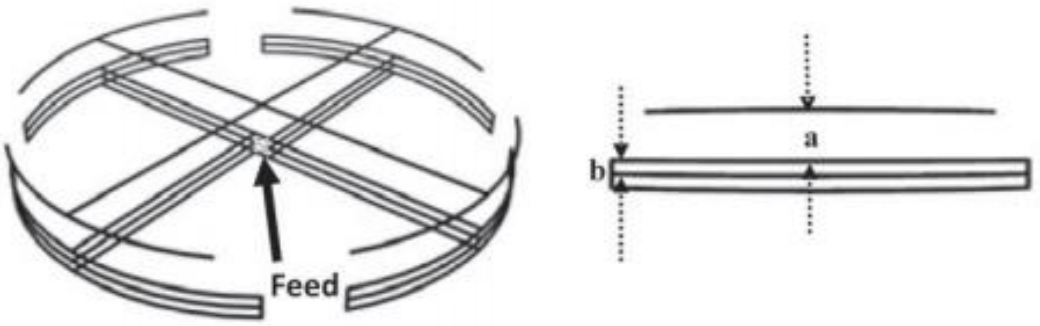

Figure 6. Wire dipole antenna with folds [6].

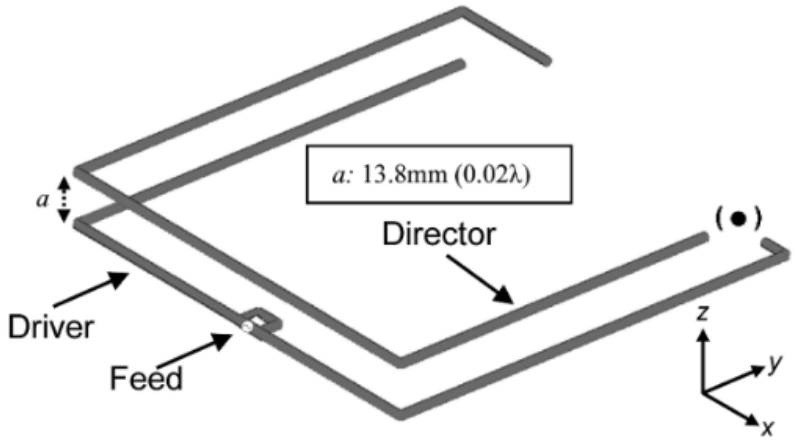

Figure 7. RFID antenna with T-matching [7].

1.5 Planar Antennas

In recent years, antennas that are printed or planar have become admirable in many applications. The appeal of planar antennas lies in their low cost, easy fabrication, low profile, and their easy integration with circuits and lumped elements. Some common antennas that are planar are Planar Inverted-F Antennas (PIFA), patch antennas, and slot antennas. Patch antennas are common in mobile phones and consist of a patch of metal over a ground plane separated by a dielectric material known as a substrate. The simplest design of a rectangular patch can be used, but further design changes to the patch can produce circular polarization. Some CP patch designs are shown in Figure 8.

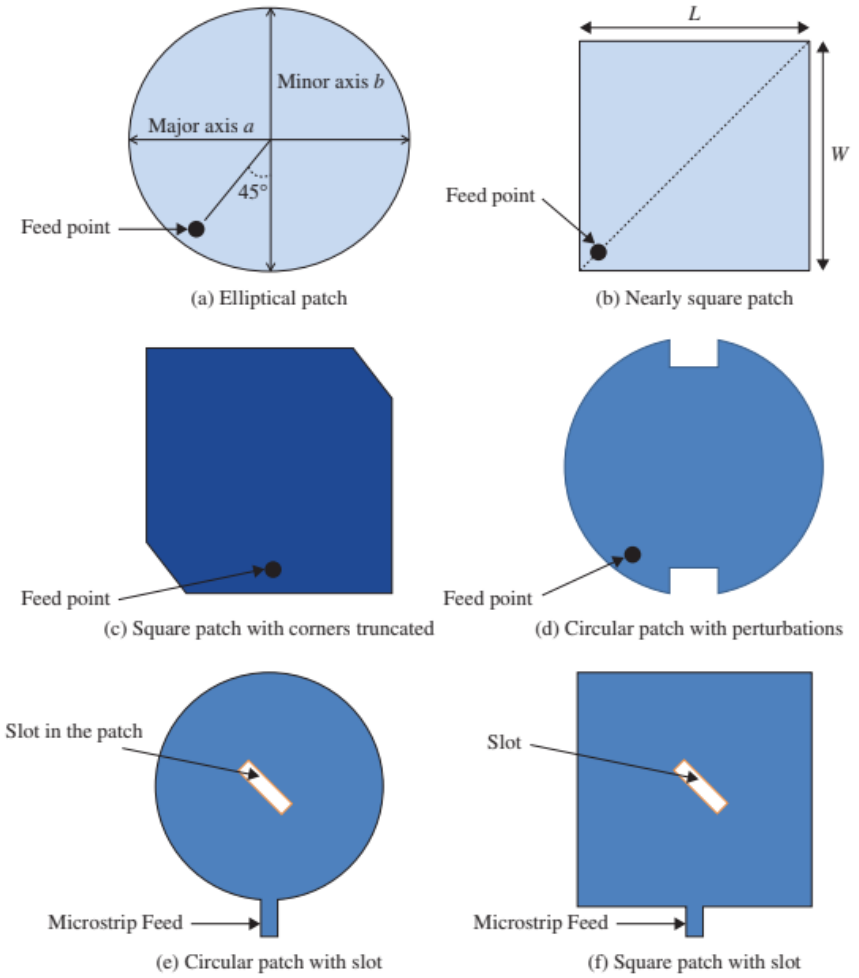

Figure 8. Patch antenna designs that produce circular polarization [8].

Basic antennas like the λ/2 dipole antenna can be easily converted to a planar design by printing it on a substrate such as FR-4 or Duroid, the only difference that must be made is to the width of the dipole arms. For example, if a wire λ/2 dipole is constructed with AWG 18 copper wire (0.5118 mm radius), the planar equivalent will have a width of 2 mm (nearly 2 times the width of the wire version).

1.6 Antenna Measurement Tools

After simulation and optimization is done in computer software, antennas are fabricated and measured to provide verification of simulated antennas. All measurements are performed in an anechoic chamber that can take measurements from 1 to 40 GHz. Aluminum sheets and foam absorbers cover the walls of the chamber, to work as a faraday cage and reduce reflections, respectively. Two TDK horn antennas are used

for reference as they have known antenna parameters for realized gain, thus they can be used to calculate a measured antenna's far-field parameters.

An Agilent E5063A Network Analyzer is used to measure and record the S_{11} and S_{21}. As previously mentioned, the S_{11} is used for the calculation of impedance bandwidth, while the S_{21} is used for calculations for far-field results like axial ratio, realized gain, and radiation patterns. The network analyzer used for measurements is shown in Figure 9.

Figure 9. Agilent E5063A Network Analyzer.

For circular polarization radiation patterns, the antenna under test must be rotated along its vertical axis in four scenarios, two rotations for the XZ plane and two rotations for the YZ plane. One rotation of each of these planes is the co-pol, and the other is the cross-pol which correspond to the orientation of the dipole element inside of the horn antenna. With the magnitude and phase of the S_{21} data from the four rotations, the radiation patterns can be calculated and plotted using a MATLAB code that uses equation 9 to calculate the RHCP or LHCP patterns at each frequency and rotation angle. Subscript *A* corresponds to the magnitude of S_{21}, subscript *P* corresponds to the phase, while the *H* and *V* represent the co-pol and cross-pol rotations, respectively.

$$E_{RH\ or\ LH} = \frac{1}{\sqrt{2}}\{[H_A \cos(H_p) + V_A \sin(V_p)] + j[H_A \sin(H_p) - V_A \cos(V_p)]\}$$

Equation 9. Calculation for representing RHCP or LHCP patterns from measurement data [9]

Through simulation, the environment and fabrication of the antenna are under perfect conditions but for measurement that is not the case. Fabrications errors and the area surrounding the antenna produce error so steps must be taken to reduce this error in measurements. One way to reduce error is to use a balun to reduce the imbalanced power being applied to the antenna. There are many types of baluns, but the two that are used for measurements in this thesis are the quarter-wavelength and hybrid baluns. The quarter-wavelength balun is a quarter-wavelength long wire that connects the outer conductor of the coaxial cable to a portion of the antenna fed by the inner conductor. On the other hand, a hybrid balun is a commercially available tool that equally balances the powering being fed to the antenna and is primarily used for broadband antenna measurements. These two types of baluns can be seen in Figure 10 and Figure 11, respectively.

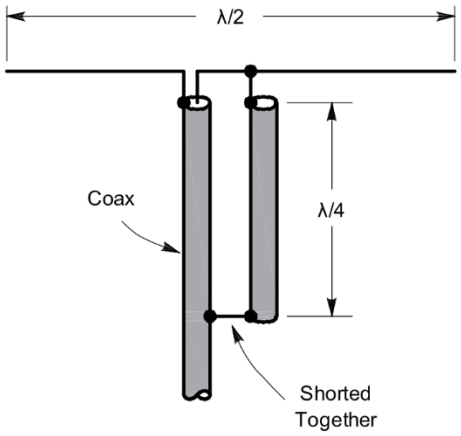

Figure 10. Quarter-wavelength balun.

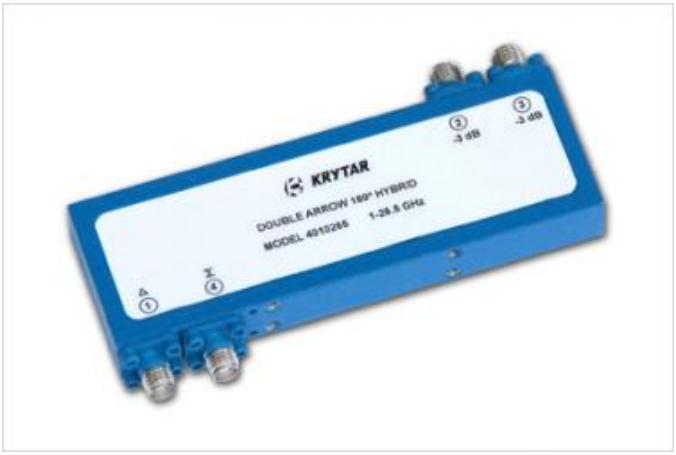

Figure 11. Krytar 180-Degree hybrid balun.

The measurements are conducted in an anechoic chamber covered in foam absorbers and metal sheets. The absorbers reduce noise reflection that may skew results, while the metal sheets work as a Faraday cage to block out electromagnetic signals that may interfere with the antenna measurements. The inside of the anechoic chamber is shown in Figure 12. The horn antenna is placed far enough away from the antenna rotator to ensure that the results are from the far-field radiation and not from the near-field radiation.

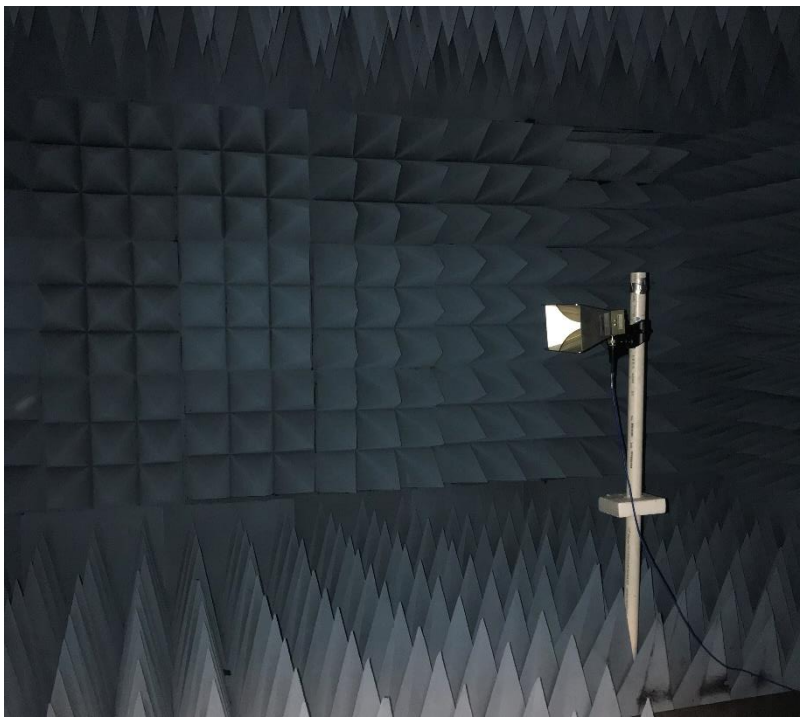

Figure 12. Anechoic chamber setup.

1.7 Objectives

The objective of this thesis is to reduce the size of circularly polarized antennas with bidirectional propagation. Reduction of size in antennas is necessary for modern communications systems as electronic devices get smaller. While circular polarization reduces the losses associated with orientation and polarization mismatch that is common in LP antennas. Also, methods for extending the bandwidth into the broadband category are investigated as they pertain to modern printed antennas for bidirectional communication scenarios.

CHAPTER 2

DESIGN OF AN ELECTRICALLY SMALL, CLOSELY-SPACED, CIRCULARLY POLARIZED, PARASITIC ARRAY WITH PATTERN RECONFIGURABILITY FOR BIDIRECTIONALITY

2.1 Introduction

Yagi antennas have been reliable in wireless communication systems for nearly 100 years. Their design procedure has been laid out by Viezbicke in [4] for high directivity. To further increase the appeal of the yagi structure, circular polarization has been introduced in a single feed design by having differing lengths on the vertical and horizontal elements. This procedure is accurately described in [3] by generating a 90° phase difference between the input admittance of the two vertical and horizontal dipole arms. The main drawback of the yagi antenna is the physical size that is caused by the nearly 0.2λ spacing between the elements, so size reduction is sought after in practical applications. One metric that is used to accurately compare the size of antennas operating at different frequencies is the electrical size or *kr*. This value is composed of the wave number, *k*, and the radius, *r*, of the smallest sphere that is capable of fully enclosing the antenna geometry. Electrically small antennas are classified as such if they have a *kr* less than 1, but smaller values are capable but begin to have diminished results when the value is less than 0.8 [10].

Commonly, size reduction in yagi antennas can be achieved by one of two means. First, top loading on ends of the dipole arms has been used to reduce the overall volume [11]. The best-case scenario is when the top loading is arced to follow the radius of a sphere while maintaining the same electrical length and thus resonant frequency. Secondly, the spacing between the elements can be reduced down to the magnitude of 0.02λ and an electrical size of 0.84 can be achieved but with diminished results as this close of spacing dramatically reduces the radiation resistance [6]. Reduced radiation resistance provides poor matching to characteristic impedance, so methods must be implemented to boost the radiation resistance when these size reduction techniques are introduced.

One of the most common methods to boost the radiation resistance to match with characteristic impedance is the use of folding [12]. This technique involves adding folding the ends of the dipole arms

and with multiple folds further increasing the radiation resistance. This procedure is simple and easy to replicate but does risk an increase in *kr* since the sphere enclosing the antenna may become larger if the multiple folds are necessary. Similarly, t-matching can be introduced around the feed to boost the radiation resistance [7]. T-matching is commonly employed on RFID antennas for its convenient radiation boost [13, 14].

Many antennas have been designed for unidirectional propagation that is traditionally admirable in point-to-point communication, but few have been introduced for long and narrow bidirectional scenarios like subways, bridges, streets, and tunnels. Bidirectional propagation is necessary in these destinations as obstacles are present in perpendicular directions. To produce a bidirectional pattern, parasitic elements can be turned on and off using a switch to direct the realized gain in two opposing directions [15]. PIN diodes are commonly used as switches for these antenna designs as they can prevent current in parasitic elements when no power is supplied.

In this paper a bidirectional, circularly polarized parasitic array is proposed with a small electrically size. First, the antenna design is taken through three iterations to show how each structure effects the antennas characteristics. Next, the two-element parasitic array is converted to a reconfigurable design by duplicating and mirroring the director on the other side of the driver. Thirdly, a Genetic Algorithm is used to optimize the antenna design for high realized gain and axial ratio in the propagation direction. Then, a circuit is constructed to switch the active director with the use of a single battery cell. Finally, the three element array is simulated in FEKO to verify that the inactive element has little effect on the radiation results observed through optimization.

2.2 Antenna Design Procedure

The design procedure for the proposed antenna can be seen in Figure 13 with three separate design iterations. Each antenna is designed using 12 AWG (1.02616 mm radius) copper wire in FEKO simulation software, with accompanying realized gain and axial ratio, in propagation direction ($+z$), of each step shown in Figure 14 and Figure 15, respectively. Minor design changes are implemented between each iteration to reduce electrical size, while maintaining high realized gain and circular polarization.

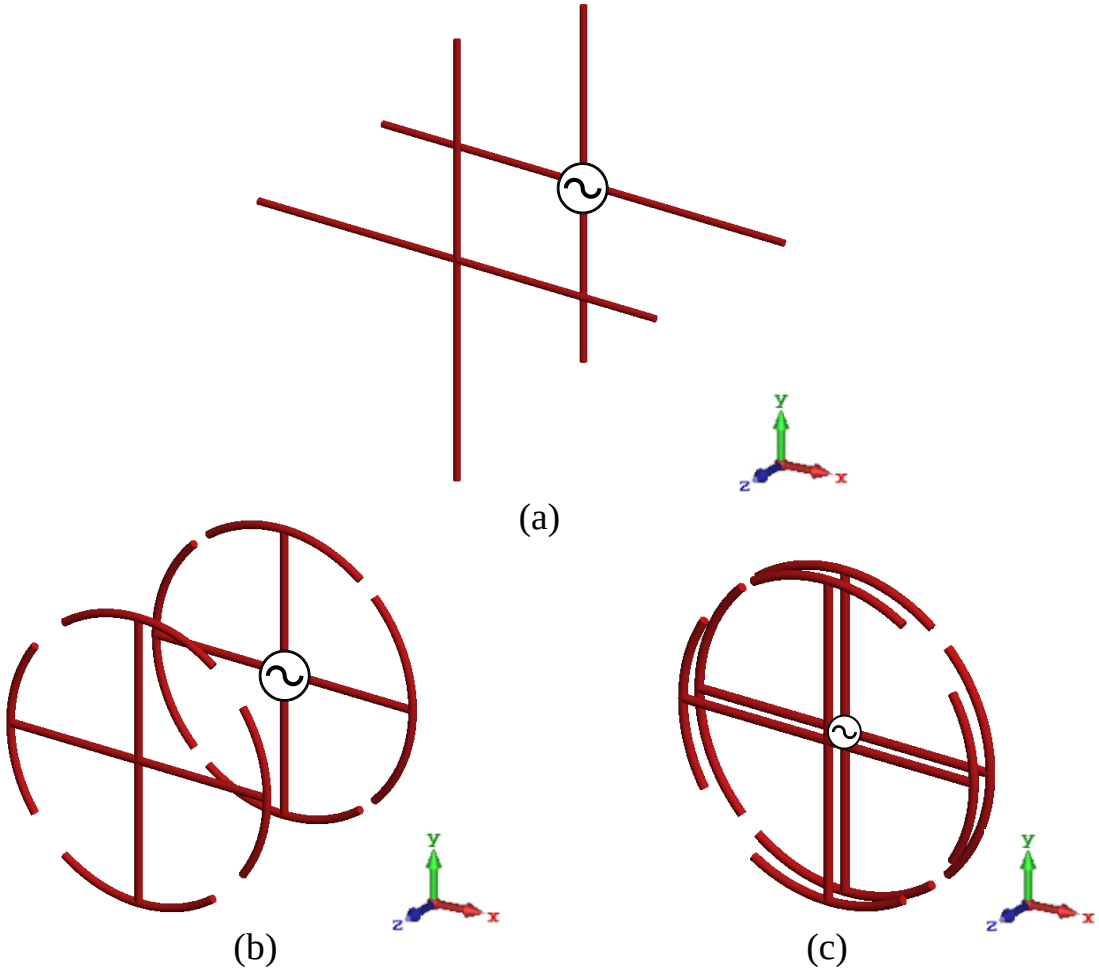

Figure 13. Design iterations. (a) 0.2λ spacing two element yagi antenna. (b) Top loaded 0.2λ spaced two element yagi antenna. (c) 0.02λ spaced two element yagi with top loading for 0.78 kr.

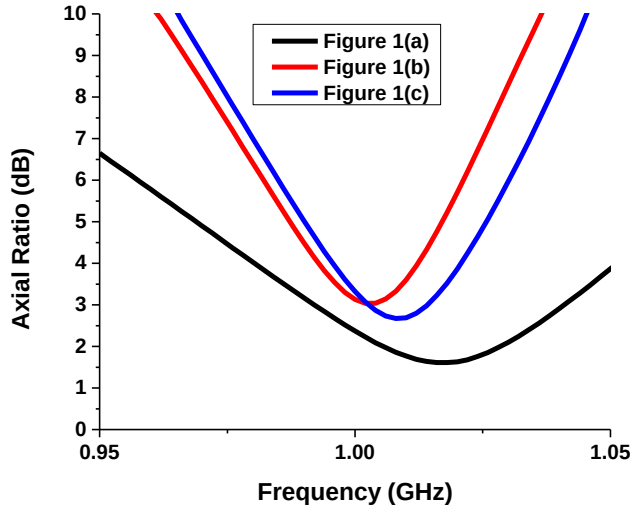

Figure 14. Realized gain (in +z direction) of the design iterations of Figure X.

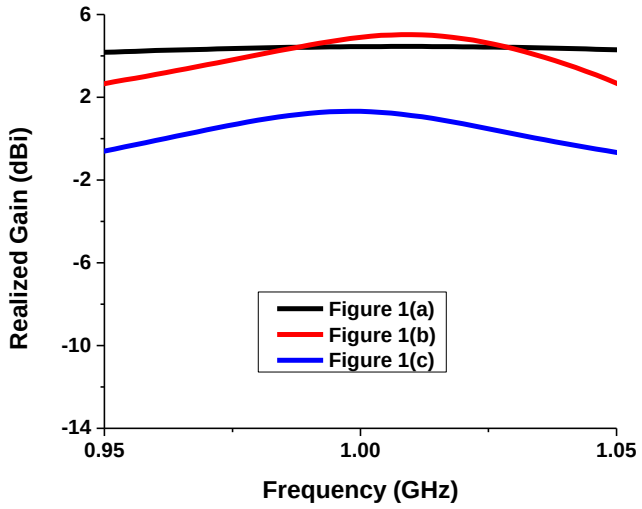

Figure 15. Axial ratio (in +*z* direction) of the design iterations of Figure X.

First, a full-sized, two element, CP, Yagi antenna is shown in Figure 13(a). The driver's vertical dipole arm is roughly 80% of the horizontal dipole arm length to provide CP, while the director's vertical and horizontal dipole lengths are shorter than the driver to increase realized gain in the propagation direction. The full-sized, 2-element, Yagi antenna has a large electrical size of 1.87, calculated at 1 GHz, due to the inner element spacing of nearly 0.2λ for optimal design structure provided by Viezbicke in [4].

Next, size-reduction is realized in Figure 13(b) by adding arced top loading on the ends of the driver and director elements. The spacing is maintained at 0.2λ to prevent reduction in radiation resistance, allowing for a kr of 1.47. At this stage, the antenna achieves a peak realized gain of 5 dBi, while just barely reaching 3-dB axial ratio.

Then, the electrical size is further reduced to 0.78 by decreasing the inner element spacing to 0.02λ. The axial ratio is maintained below 3 dB. It is noted that the realized gain at this step is reduced by 3 dBi as the mismatching losses are high, which is caused by the reduced radiation resistance from close spacing and the *kr* less than 0.8.

To counteract the drop in radiation resistance, matching stubs are attached symmetrically around the feed. The matching stub is made of 18 AWG (0.5118 mm radius) copper wire, and connects the vertical and horizontal dipole arms of the driver. Matching stubs are commonly used to boost the radiation resistance

of RFID antennas. A genetic algorithm (GA) was used in FEKO simulation software to find the optimal dimensions for the proposed antenna. The dipole radius, inner element spacing, and feed spacing were kept constant while the vertical and horizontal angles of the driver and director and stub matching length were varied for optimization. As the antenna is intended for CP and high gain, the GA searched for parameters that achieved an axial ratio less than 1.5 dB and a realized gain greater than 6 dBi at 1 GHz. A cost function weight ratio of 1:2 (axial ratio : realized gain) is used for the GA after tests to find the correct values. The final, 2-element array is shown in Figure 16 with parameters chosen by the GA that produced the lowest cost function.

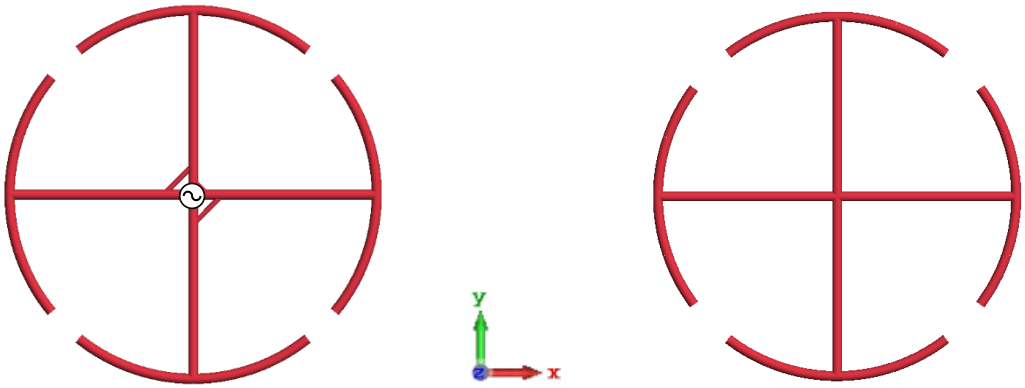

Figure 16. Antenna design after GA. (a) Driver and (b) director.

2.3 Implementation of PIN Diode Switch Circuit

The previously discussed, optimized antenna is intended for pattern reconfigurability by introducing mirroring the director on the opposite side of the driver. A switching circuit is then used to choose front or back propagation, by selecting which director to turn on/off. The switching circuit is a combination of four PIN diodes as shown in Figure 17. The orientation of the PIN diodes allow for a voltage source to switch on a single director, thus providing bidirectional propagation with high gain.

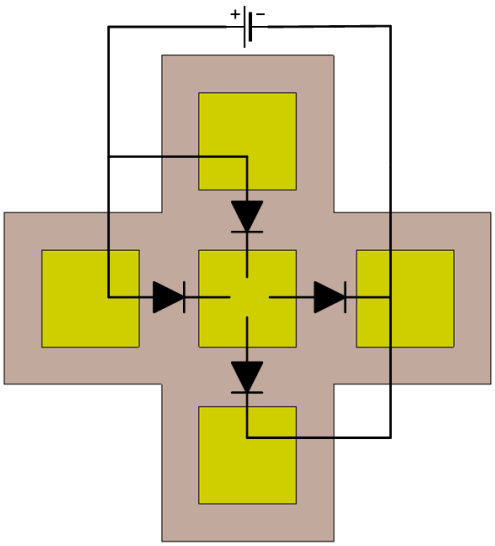

Figure 17. PIN diode switch circuit for controlling director.

The switching circuit is milled onto commercially available FR4 with a 1.6 mm thickness, dielectric constant of 4.4, and loss tangent of 0.02. A prototype is of the circuit is shown in Figure 18, with accompanying PIN diodes soldered on in the same orientation previously discussed. The PIN diodes have a forward voltage of 0.95 V and a continuous forward current of 50 mA. A 1.5-volt button cell battery in series with a 51 Ω is used to power the PIN diodes while lowering the current across them to prevent damage to the electronic components.

2.4 Results and Discussion

Since FEKO software cannot simulate the switching circuit, a 5 mm cut is taken from the center of the inactive director, as seen in Figure 19, to test its effect on antenna propagation. The resulting S_{11}, axial ratio, and realized gain with the front director on and the back director on are shown in Figure 20, 21, and 22, respectively. With the cut taken from the directors, the director's electrical length is no longer near the driver's electrical length causing little effect on the antenna's operating characteristics.

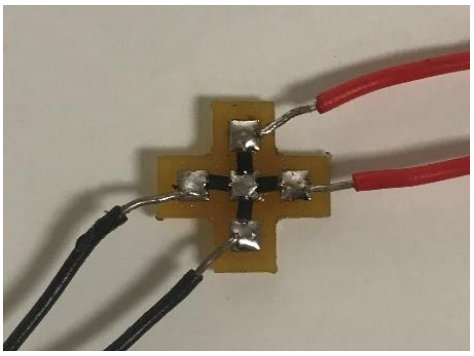

Figure 18. Prototype of the PIN diode switch circuit.

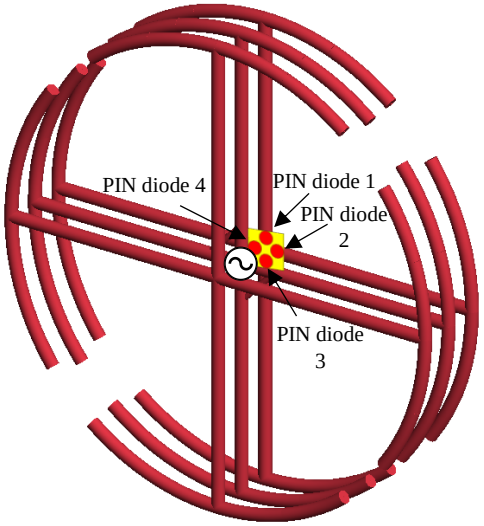

Figure 19. FEKO simulation, with -*z* driver cut by 5 mm.

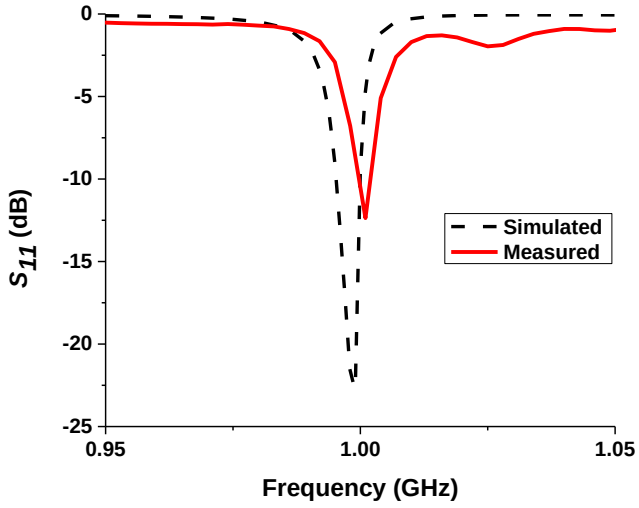

Figure 20. Simulated and measured S_{11} of the optimized antenna.

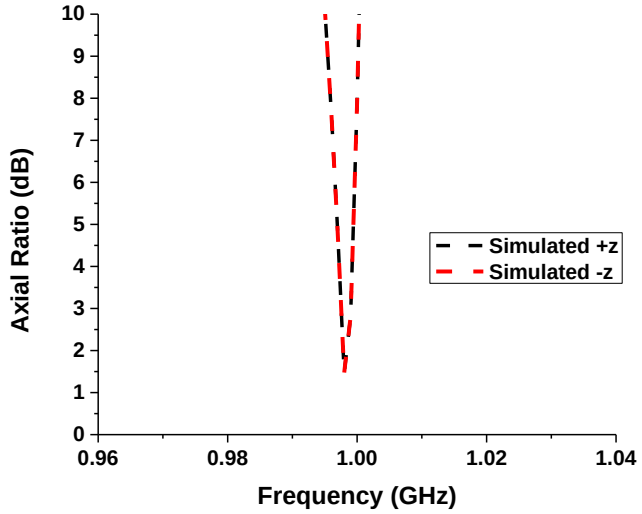

Figure 21. Simulated axial ratio in propagation direction corresponding to the active director.

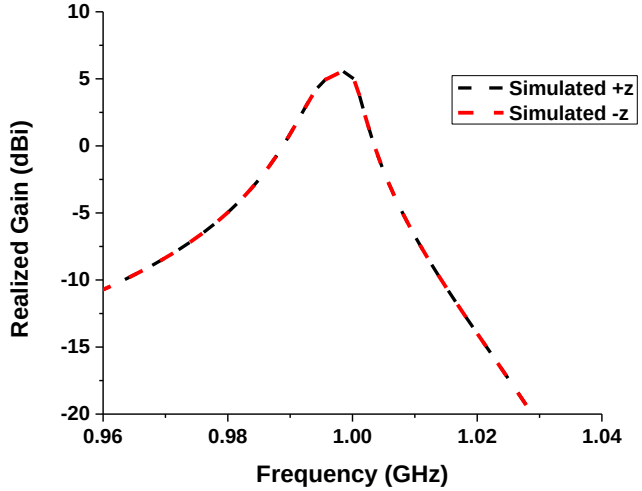

Figure 22. Simulated realized gain in propagation direction corresponding to the active director.

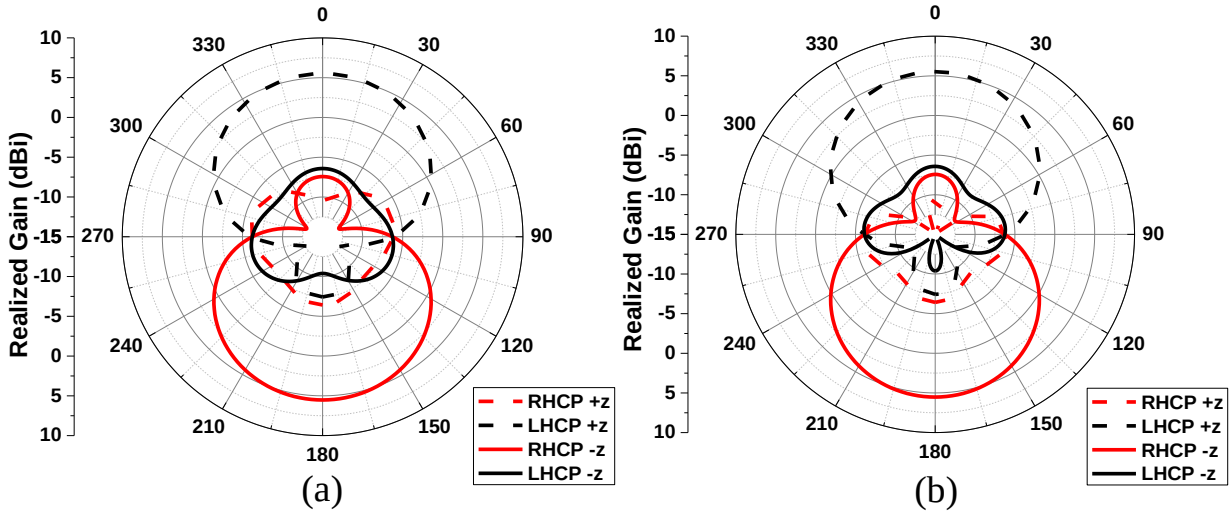

Figure 23. Simulated radiation pattern at 1 GHz in the (a) XZ plane and (b) YZ plane.

The radiation patterns at 1 GHz are presented in Figure 23. In both XZ and YZ planes, the right-handed and left-handed magnitude are similar proving the antennas bidirectional nature through the implementation of an electronic switch to control the direction of propagation.

2.5 Conclusion

A pattern reconfigurable, circularly polarized, electrically small parasitic array is proposed with a switch circuit to electrically change the propagation direction for use in bidirectional communication paths. The antenna achieves a 0.78 *kr* with a peak realized gain of 5.6 dBi. The antenna array is conformal with an overall thickness of 0.04λ and maintains a common bandwidth in both propagation states. The proposed antenna has possible applications in subways, tunnels, bridges, and streets where bidirectional communication is necessary with high realized gain.

CHAPTER 3

DESIGN OF AN ELECTRICALLY SMALL, BIDIRECTIONAL, PRINTED, CIRCULARLY POLARIZED CROSS DIPOLE

3.1 Introduction

Research of planar antennas has become integral to meet today's need for size reduced electronics. Their conformal design and inexpensive structure make them admirable for applications in consumer devices. To further increase their appeal, work has been done to reduce the electrical size of planar antennas to make them electrically small. Electrically small antennas ($kr < 1$) use less space with respect to their resonant wavelength than their full-sized counterparts but suffer from a lower radiation efficiency and impedance bandwidth product [10,16,17]. Planar size reduction can be achieved by use of spiral [18], meander [19], and top-loading designs [11]. Multiple folds and capacitively coupled parasitic elements have been used to counteract the negative effects of electrically small antennas [6,20,21,22].

Another characteristic that is desired for communication systems is circular polarization (CP) as these types of antennas lower the effect of polarization mismatch and multipath interference. Crossed dipoles have been designed to produce CP by having unequal vertical and horizontal lengths [3]. Several circularly polarized cross dipoles have been created that are electrically small by implementing Huygens dipoles and near-field resonant parasitic elements [23,24,25]. Previously, a circularly polarized antenna with an electrical size, kr (k is the wave number and r is a radius of a sphere to enclose the antenna), of 0.75 was achieved in a two-element parasitic array with pushed/pulled elements. This antenna implements T-matching near the feed to boost the input resistance to match with 50-Ω characteristic impedance [7]. Although the previously mentioned two-element antenna and Huygens dipoles have thin structures they are not truly planar as they contain a director or multilayered components to generate a unidirectional radiation pattern.

Bidirectional propagation is necessary in long and narrow communication paths. Tunnels, subways, and streets benefit from bidirectional antennas as they are two-way communication scenarios with obstacles orthogonal to the propagation direction. CP bidirectionality has been achieved in planar monopole antennas

with modified geometry [26,27], but these antennas are wideband and are not designed for an electrically small size. A pattern reconfigurable Huygens dipole with a bidirectional state has been designed that is linearly polarized with a kr of 0.98 [28]. An antenna has been designed for a CubeSat satellite that achieves CP, bidirectionality, and kr of 0.94 [29].

In this communication, a printed, CP cross dipole is designed for use in bidirectional communication scenarios while maintaining an electrically small size. First, the design procedure is presented in five steps through CST microwave studio simulation software to show the alterations taken to produce the desired antenna characteristics. Secondly, square t-matching stubs are implemented around the feed to boost the low radiation resistance that is produced from the low *kr*. Then, a genetic algorithm (GA) is used to find the optimal antenna dimensions to provide the broadest CBW while maintaining a 0.65 *kr*. Next, a surface current study is shown to describe and understand the generation of CP in the antenna design. Finally, the proposed antenna is fabricated and measured to verify the results obtained in simulation.

3.2 Antenna Design Procedure

The design hierarchy for the design of the antenna is shown in Figure 24. Five steps are taken to show the progression of S_{11} and axial ratio as the antenna is altered for a CP, printable, electrically small design. The S_{11} and axial ratio at each iteration is shown in Figure 25 and Figure 26, respectively.

First, as shown in Figure 24(a), a cross dipole with identical arm lengths is designed at 1.5 GHz using AWG-18 wire (radius of 0.5 mm). With the four dipole arms being the same length, no CP is generated with an axial ratio value of 40 dB. This iteration is linearly polarized and has a *kr* of 1.4, so modifications are taken to generate CP.

Next, the dipole arm lengths are differed to produce CP. The long and short dipole arms are 52 mm and 41.6 mm in length, respectively. These lengths provide a length difference of 80%, which is capable of producing an axial ratio less than 3 dB at 1.5 GHz. The *kr* is increased to 1.6, due to the long and short dipole arms resonating at two separate frequencies. The separate resonances allow for the generation of CP by producing a 90-degree phase difference between the input admittance angles. Since the two dipoles no longer resonate at the same frequency, the -10-dB IBW is more than doubled at 28.9%.

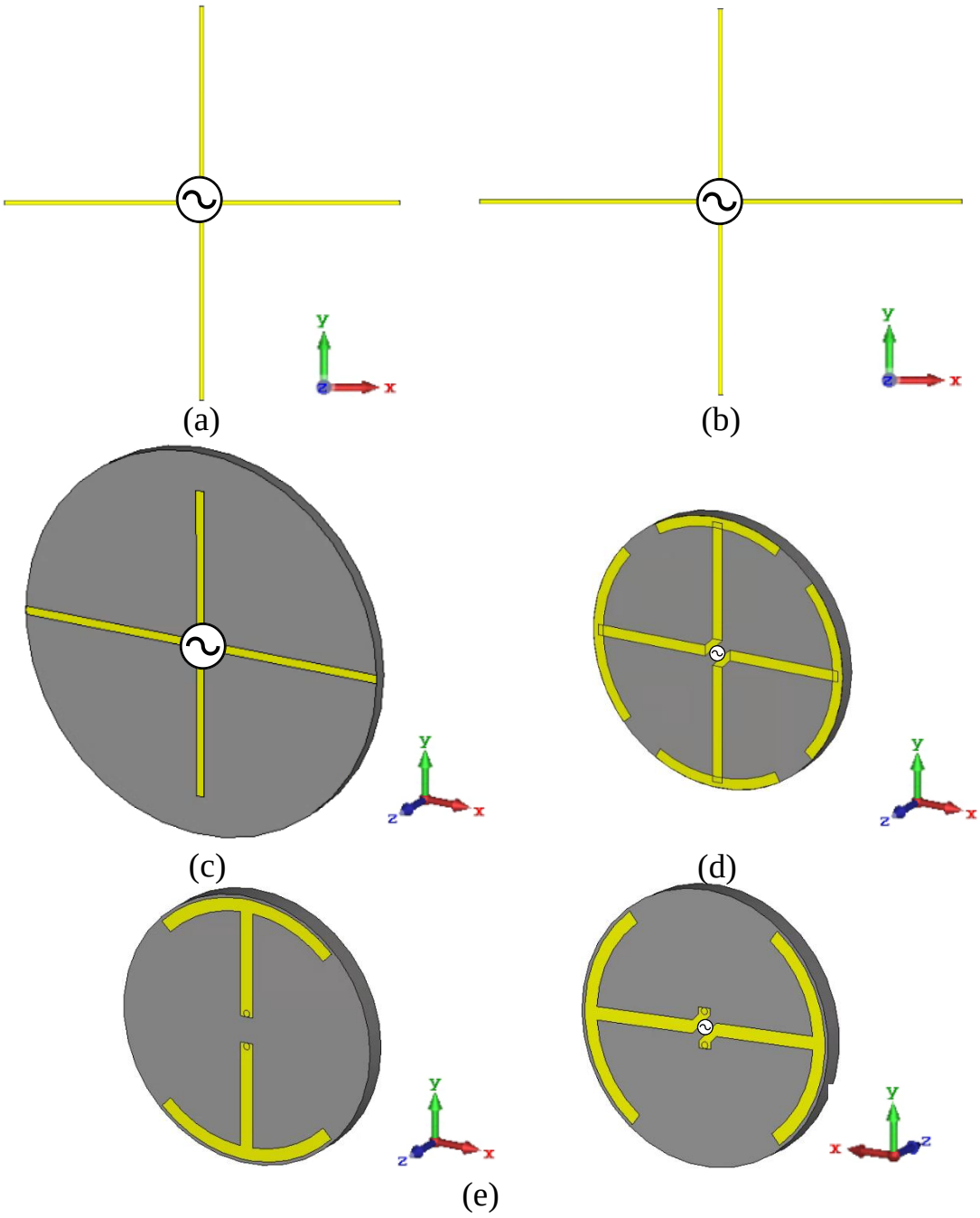

Figure 24. Antenna design hierarchy. (a) Full sized, wire, cross dipole. (b) Full sized, wire, CP, cross dipole. (c) Full size, planar, CP, cross dipole. (d) 0.8 *kr*, planar, CP, cross dipole. (e) 0.65 *kr*, two-sided, cross dipole.

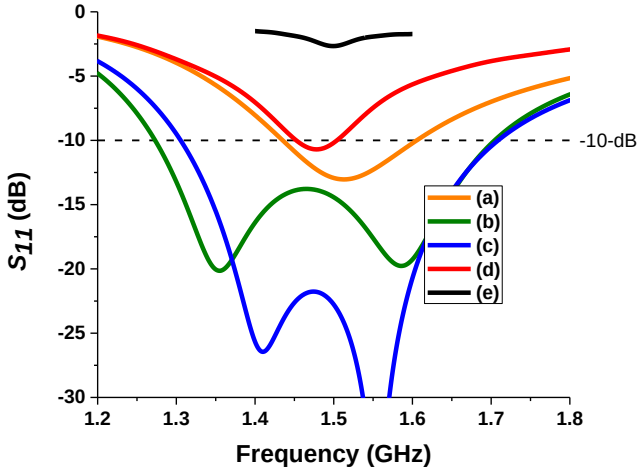

Figure 25. Simulated S_{11} of the antenna designs in Figure 24.

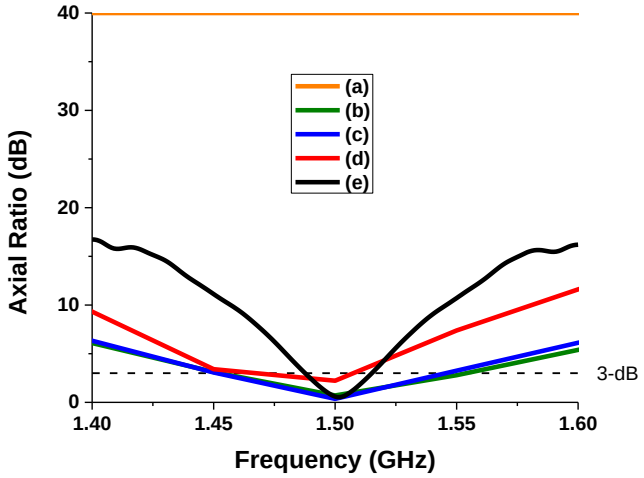

Figure 26. Simulated axial ratio of the antenna designs in Figure 24.

Then, the antenna is converted to a planar design that is printed on Rogers 5880 with a thickness of 3.2 mm, dielectric constant of 2.2, and loss tangent of 0.0009. The dipole arms are given a width of 2 mm, which is roughly 4 times the radius of the wire version to achieve proper matching. Also, the lengths of the dipole arms are reduced to 45 mm and 36 mm as a frequency shift occurs from placing the antenna on a substrate. The planarization of the design lowers the *kr* to 1.42, while still producing a similar -10-dB IBW and 3-dB ARBW as the full-size wire antenna previously discussed.

Following the conversion of the cross dipole to a planar design, the antenna is size reduced to 0.8 *kr* using arced top loading on the ends of the dipole arms. The straight dipole arm lengths are kept the same to maintain a circular design and reduce the size, so the top loading angles are differed to produce CP. One

can see that the IBW and ARBW are diminished at this stage, as the radiation resistance is beginning to drop from the electrical small size. Subsequently, further size reduction will reduce the radiation resistance too low providing worse matching to 50 Ω characteristic impedance completely removing the IBW. Also, for a smaller electrical size, the radius of the structure must be reduced by 4.8 mm while maintaining resonance at 1.5 GHz. At this size, the top loading arcs begin to intersect, as they must become longer to compensate for the smaller radius.

Finally, the antenna design utilizes both sides of the Roger 5880 substrate to be two-sided printable with a 0.65 *kr*. Since there is no electrical connection between the front and back sides of the antenna, AWG-18 wire shorting pins are introduced through the material to connect the vertical and horizontal dipole arms. The ARBW is similar to the previous step, but the -10-dB IBW has disappeared as the Rin is decreased to 7.8 Ω which does not provide adequate matching to characteristic impedance. The arced top loadings do overlap at this *kr*, but since they are on different sides it does not affect antenna performance. The antenna at this iteration does produce a bidirectional pattern, but with poor matching the realized gain is low.

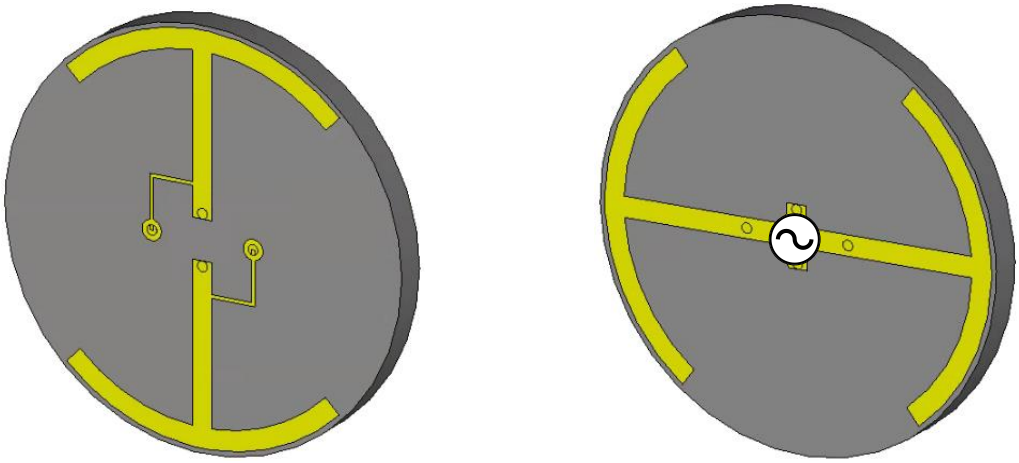

(a) (b)

Figure 27. Final optimized antenna design. (a) Front side and (b) backside.

To counteract the reduced input resistance, square t-matching is implemented near the feed on the final antenna design shown in Figure 27. Similar to the shorting pins used to connect the two dipole arms, shorting pins are used at the end of the t-matching to connect it to both sides of the antenna. A GA is used to find the optimal t-matching length and width for the broadest CBW around 1.5 GHz. The cost function

is given as follows:

$$Cost = \sum_{i=1}^{5} \{(S_i + 14) + (AR_i)\} \text{ [dB]}$$

Where S_i is S_{11} and AR_i is the axial ratio at discrete frequency points. The discrete points are five evenly spaced frequency values from 1.48 to 1.52 GHz. The weight ratio between the two goals is constant at 1:1, only the target for each goal is different at -14 dB for S_{11} and 0 dB for axial ratio. A square design is used for the t-matching to maintain symmetry which is important for CP.

The surface current at 1.5 GHz is shown in Figure 28 to explain the generation of CP. The surface current is shown at four different phases, starting at 0º and increasing by 90º increments until 270º. The current is only shown on the copper, and the substrate is hidden so both the front and back sides can be seen at once. At 0º, the strong current is shown moving to the left, while at 90º the strong current goes up along the vertical dipole element. The same 90º rotation of strong current direction, is noticeable for all subsequent surface currents. The equal magnitude of strong current between 90º increments is a descriptor for CP, while the clockwise rotation of direction of the strong current provides the sense of polarization of LHCP out of the front (+z) of the antenna.

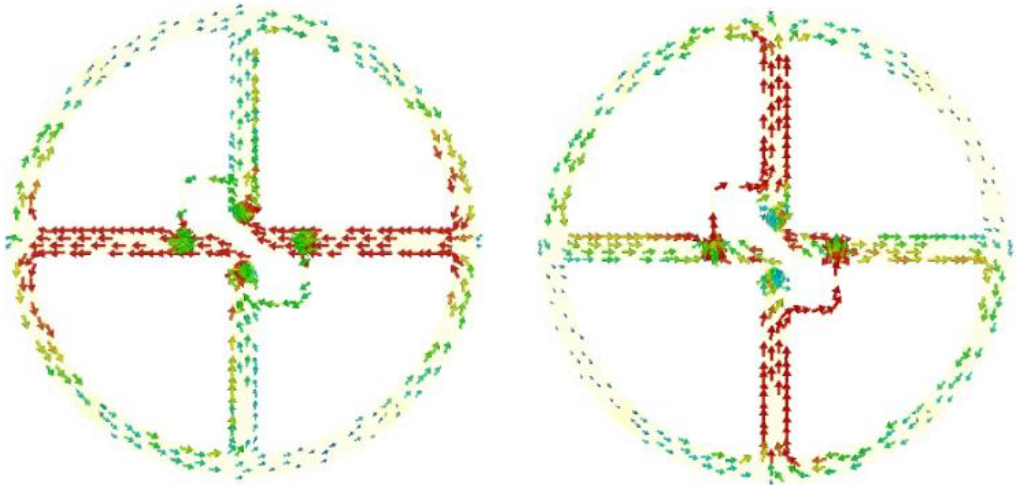

0º 90º

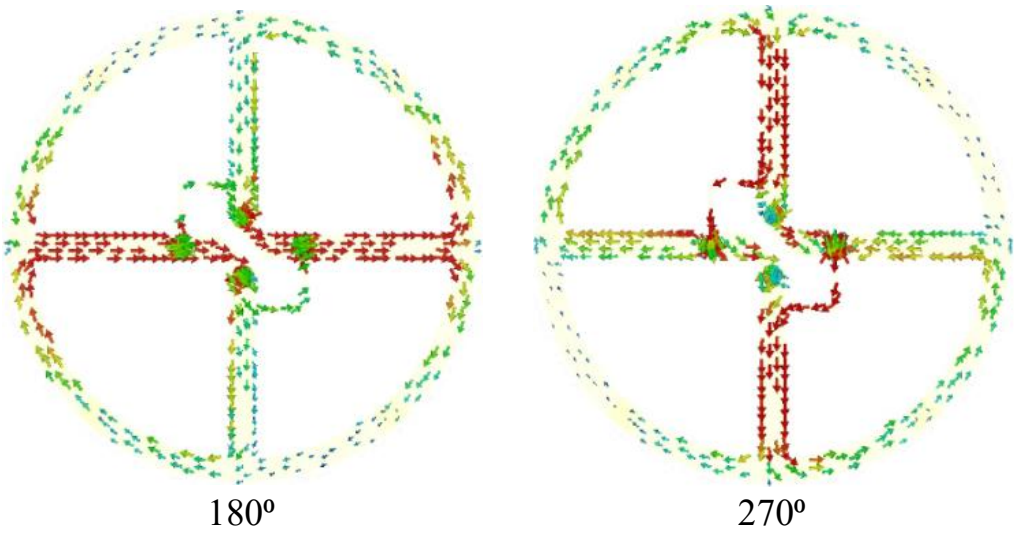

Figure 28. Surface current distribution at 1.5 GHZ at four different phases.

3.3 Results and Discussion

The final antenna design is fabricated, as shown in Figure 29, using an LPKF milling machine. To verify simulation results, the antenna is measured in an anechoic chamber using a network analyzer and a quarter wavelength balun.

The simulated and measured S_{11} and axial ratio are shown in Figure 30(a) and 30(b), respectively. A double dip is observed in simulated and measured S_{11}, which is common in CP cross dipoles. Simulation shows a CBW of 2.0%, while the measured results have a CBW of 1.5%. In Figure 31, the simulated and measured realized gain in the +z direction are overlapped, with a peak realized gain of 1.36 dBi in simulation and 1.31 dBi in measurement. Next, the radiation patterns are presented at 1.51 GHz which lies nearly in the middle of both simulated and measured CBW in both XZ and YZ planes, as shown in Figure 32. It can be seen that the antenna propagates LHCP and RHCP of equal magnitude out of the front and back of the antenna, respectively. This equal magnitude in both directions is the proof for bidirectionality which is necessary in long and narrow applications like subways, bridges, streets, and tunnels.

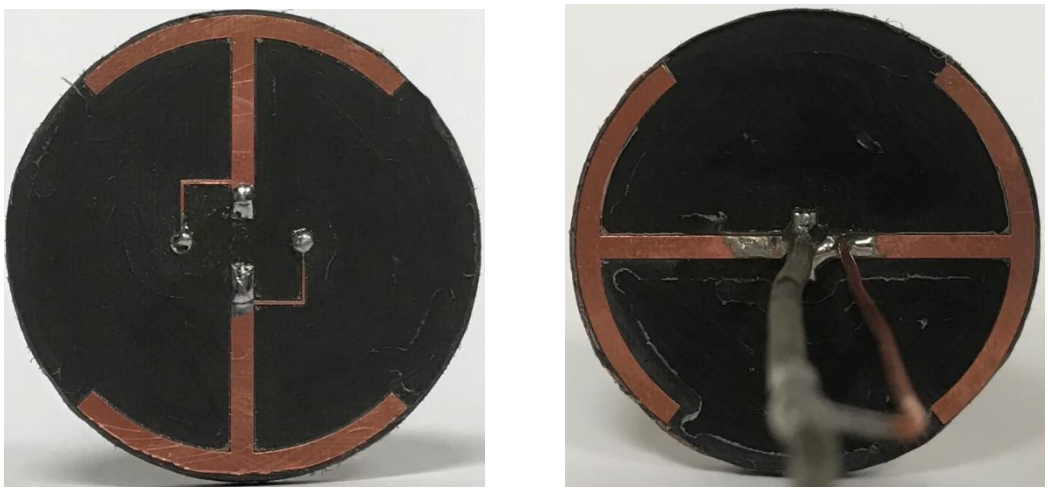

(a) (b)

Figure 29. Fabricated antenna design. (a) Frontside and (b) backside.

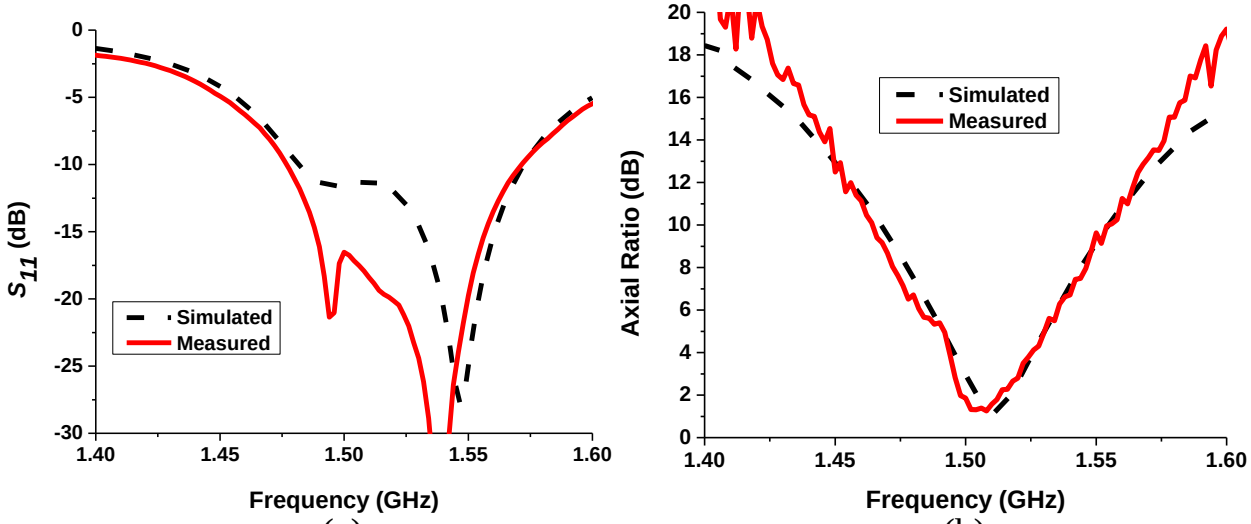

(a) (b)

Figure 30. Simulated and measured (a) S_{11} and (b) axial ratio of the optimized antenna.

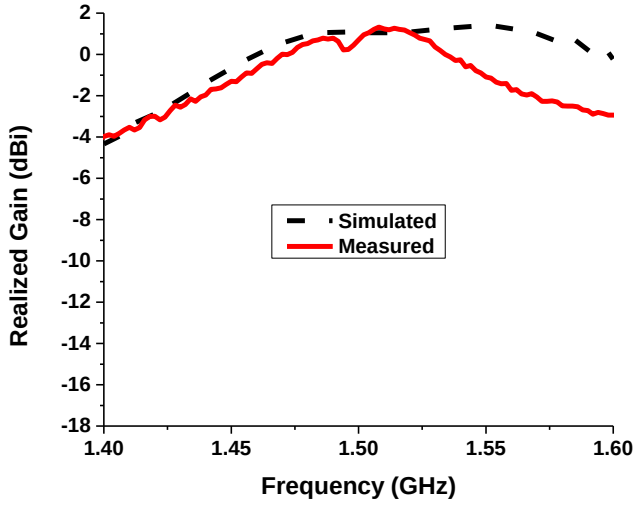

Figure 31. Simulated and measured realized gain in the +*z* direction.

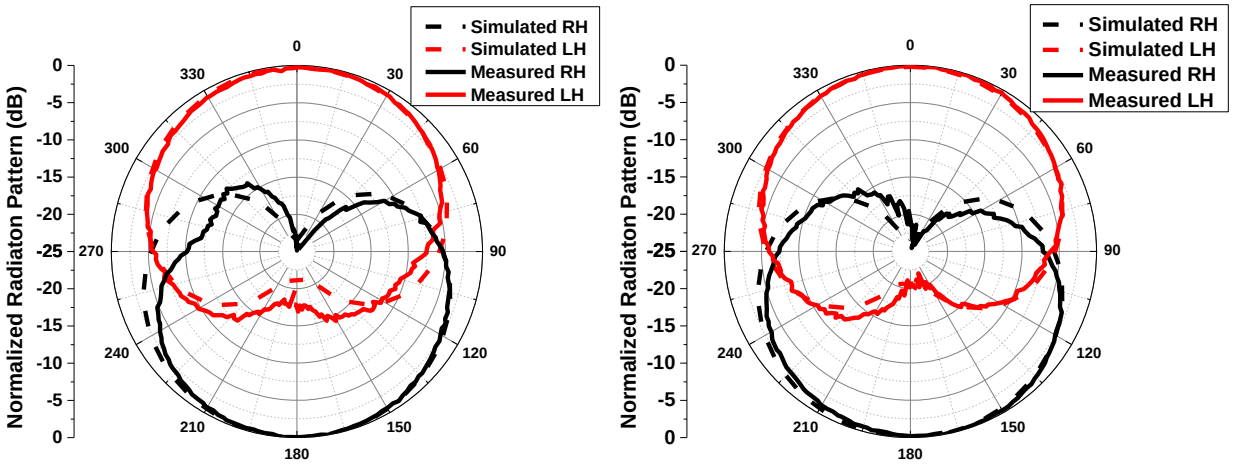

Figure 32. Simulated and measured normalized radiation patterns at 1.51 GHz in the (a) XZ plane and (b) YZ plane.

3.4 Conclusion

An electrically small, printable, bidirectional, CP cross dipole is proposed. Measurement results show little error when compared to simulation, with errors resulting from fabrication errors. The antenna achieves a *kr* of 0.65, while maintaining a bidirectional radiation pattern. Furthermore, the measured -10-dB IBW is 6.0% (from 1.478-1.57 GHz) and 3-dB ARBW is 1.5% (1.496-1.518 GHz) allowing the CBW to encompass the entire 3-dB ARBW.

CHAPTER 4

A SIZE-REDUCED, BROADBAND, BIDIRECTIONAL, CIRCULARLY POLARIZED ANTENNA

4.1 Introduction

Over decades printed antennas have been commonly used in wireless communication systems due to their low-cost structure and low profile. To further increase their appeal in the market for wireless communication systems, extensive research has been done to improve the characteristics of printed antennas for circular polarization (CP) and a broad bandwidth.

CP is used to reduce the effect of multipath interference and polarization mismatch, and a broad bandwidth allows a device to operate in the place of multiple antennas saving space in applied systems. Multiple methods have been designed that can generate CP. CP crossed dipoles as well as bent element parasitic arrays have been researched [3,6,7,30,31]. A slender helical structure with tuning of the circumference and length of the strip allows for CP [32]. Elliptical, square, hexagon, circular, and octagon shaped patches produce CP and have been analyzed [8,33]. Various techniques have been researched to extend the common bandwidth (CBW) (overlapped bandwidth between –10-dB impedance bandwidth (IBW) and 3-dB axial ratio bandwidth (ARBW)) of CP antennas. The addition of magneto-electric or stepped edges on dipole elements have been used for broadband CP crossed dipole antennas [34,35]. Broad CBWs are achieved in patch antennas with parasitic elements, shorting pins, and reactive impedance surfaces [36-38]. Also, antennas with symmetrical slots have been implemented to produce broad CBWs [39-42].

Another key metric that is important to reduce size in applications is the electrical size. The electrical size (*kr*) is a criterion that combines the wave number, k, and the radius of a sphere, r, enclosing the antenna to convey an antenna's size according to its wavelength. It is shown from the Chu limit that as *kr* gets smaller, so does the radiation efficiency and impedance bandwidth product [5,10,17]. Thus, a balance between *kr* and broad CBW is desired.

Many of the aforementioned antennas are characterized as unidirectional antennas, but bidirectional antennas are primarily used in two-way communication channels. Bidirectional antennas play important roles in long and narrow communication scenarios like subways, tunnels, bridges, and streets due to obstructions orthogonal to the communication path. Open ended slot ground planes with thin substrates have been used to achieve bidirectional radiation patterns with a broad CBW [43,44]. Monopole patches with modified geometry have been researched to make CP, bidirectional, and broadband antennas [45-47]. Also, wide-slot antenna designs with alterations to the shape of the slot and/or feedline are used to achieve broadband and CP characteristics while generating bidirectional directivity [48-53].

In this paper, a size-reduced, bidirectional antenna with CP and broad CBW is presented. Frist, the antenna is designed and simulated in CST Microwave Studio with a series of modifications to improve the CBW while minimizing the electrical size and providing bidirectionality. Then, an analysis of the optimizer is done to show how the Genetic Algorithm (GA) finds the optimum parameters for the cost function. Next, a detailed explanation of the proposed antenna structure is given for important antenna features. The current distribution of the proposed antenna is provided to analyze the generation of CP. Then the antenna is fabricated and measured to validate its CP, broadband, and bidirectional capabilities observed in simulation. The bidirectional nature of the antenna is shown through the measured radiation pattern that propagates opposite sense with equal magnitude in two opposing directions.

4.2 Antenna Design

The design procedure of the proposed antenna is shown in Figure 33. Four design iterations, step (a) through (d), are shown with variation between steps. To show the impact of each step, the S11 and axial ratio (in +z direction) vs. frequency of each step are shown in Figure 34 and Figure 35, respectively. All antennas are designed on a 54 × 54 mm2 sheet of FR4 with a thickness of 1.6 mm, dielectric constant of 4.4, and a loss tangent of 0.02.

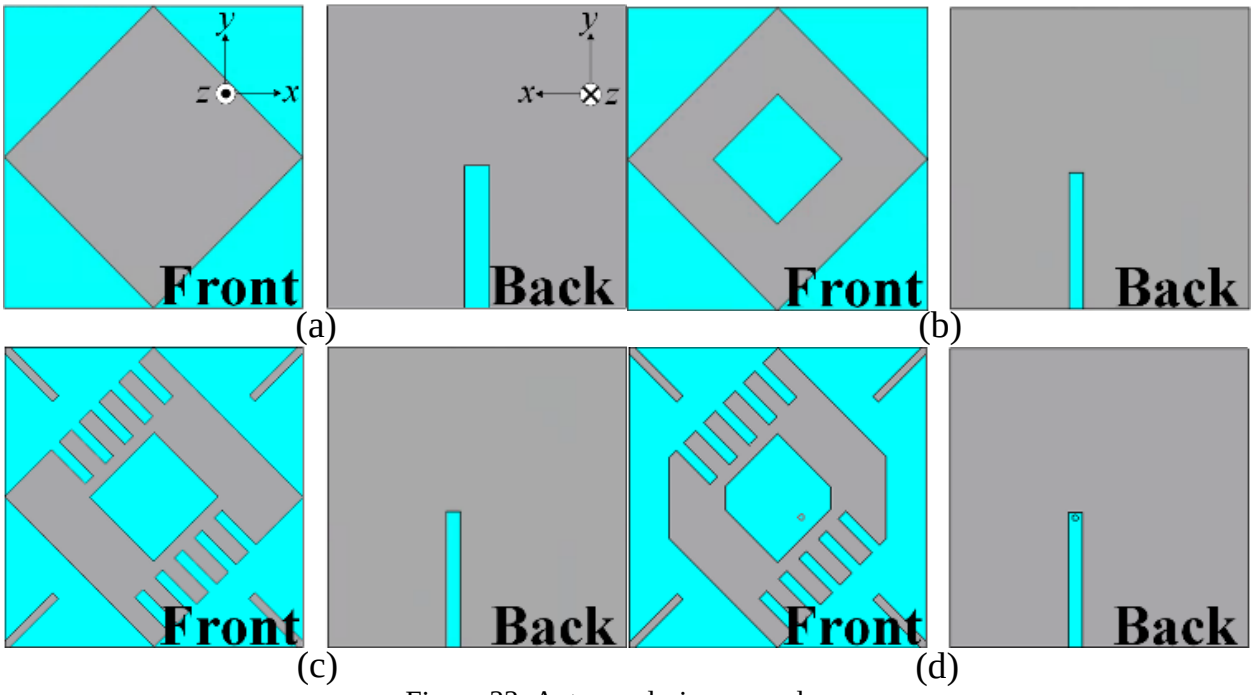

Figure 33. Antenna design procedure.

First, as shown in Figure 33(a), a rotated square slot fed by a centered feedline is used for its broadband capabilities [54]. The length of the feedline is based on the 45° rotation angle of the square slot. The side length of the wide slot is chosen to resonate at the lowest frequency possible on the 54 × 54 mm^2 sheet of FR4, as larger values will create discontinuities in the middle edges of the ground plane. The minimum S_{11} occurs at 2.64 GHz providing the antenna with a –10-dB IBW from 2.40–2.96 GHz or 20.1%. It is noted that at this step the antenna shows no feature for CP as depicted in the axial ratio of Figure 35.

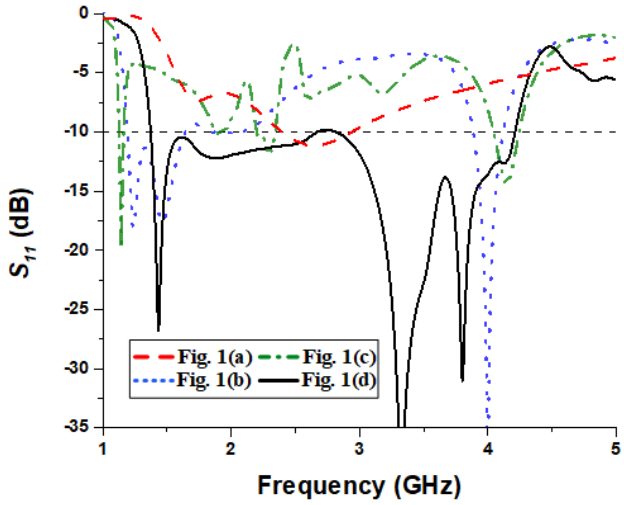

Figure 34. Simulated S_{11} vs frequency of the antenna designs in Figure 33.

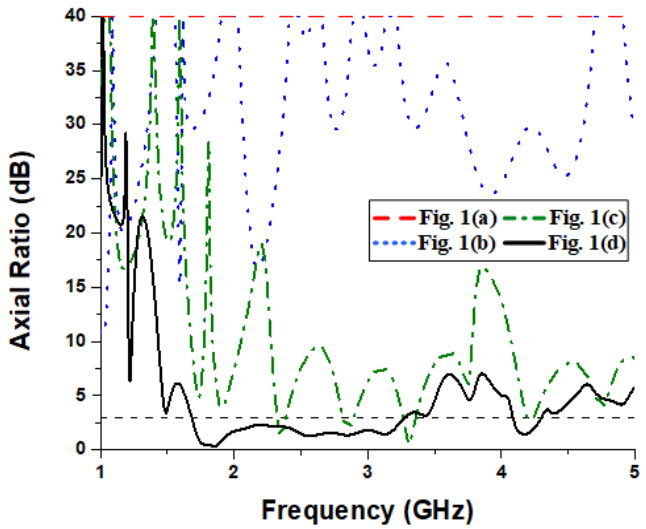

Figure 35. Simulated axial ratio vs frequency of the antenna designs in Figure 33.

Second, in Figure 33(b), a smaller, offset feedline replaces the previous feedline design, and a parasitic patch is inserted into the center of the rotated slot [55]. The new feedline extends the –10-dB IBW at the lower end by creating a dual resonance and lowers the axial ratio across the frequency range. The square parasitic patch is rotated at the same angle as the wide slot and adds a new resonant frequency at 4 GHz. The rotated parasitic square patch is used as the feeding structure for the rotated square slot, extending the current path.

Third, the design in Figure 33(c) has diagonal rectangular notches removed from the four corners of the antenna, and meander tips added to two opposing sides of the rotated slot to maintain a symmetrical design. This step reduces the axial ratio closer towards CP, seen in Figure 35, and extends the current path reducing the lowest resonant frequency.

Next, as depicted in Figure 33(d), a shorting pin is inserted between the feedline and parasitic patch [56]. Also, the two opposite, horizontal corners of the rotated square patch and rotated slot are truncated resulting in hexagonal patch and hexagonal slot, respectively. The position of the shorting pin provides broadband matching to 50-Ω, extending the –10-dB IBW drastically from the previous iteration. The placement of the shorting pin plays an integral role in matching by providing a strong current at the connection and lowering the input impedance. The truncations produce CP by generating orthogonal E-field components at the low

and high end of the –10-dB IBW [8]. The truncations in conjunction with the shorting pin provide a broad ARBW. It is confirmed that the axial ratio in the +*z* direction (forward) and -*z* direction (backward) are similar, but only the forward direction is given for brevity in Figure 35.

A GA is used in conjunction with CST software to find the optimized antenna design with the broadest CBW and highest realized gain in the forward (+*z*) direction. The cost function for the GA is defined by:

$$Cost = \sum_{i=1}^{23} \{(S_i + 20) + (AR_i - 1) + (2 - RG_i)\} \text{ [dB]}$$

Where Si is the S11, ARi is the axial ratio in the forward direction, and RGi is the realized gain in the forward direction at discrete frequency points. Although the cost function does not include results in the backward (-*z*) direction, preliminary research and tests of printed slot antennas with no ground plane prove that they have bidirectional propagation as they have no structure to direct electromagnetic waves in a single direction [54]. The frequencies for the optimizer are 23 evenly spaced values from 1.5 to 3.8 GHz. The frequency range and number of points are chosen after an initial study to find the bandwidth of the hexagonal slot and inserted hexagonal patch. In Figure 36, the value of the lowest cost function at each generation is shown. The fastest change in lowest cost function value occurs in the first 25 generations. After generation 25, there is a drop of only 0.1 dB in the next 40 generations, due to the GA finding parameter values that produce the lowest cost function value in early generations of the optimizer. Future generations begin to converge to a cost function value of 20.8 dB, so further optimizations lead to minor changes in the antenna characteristics.

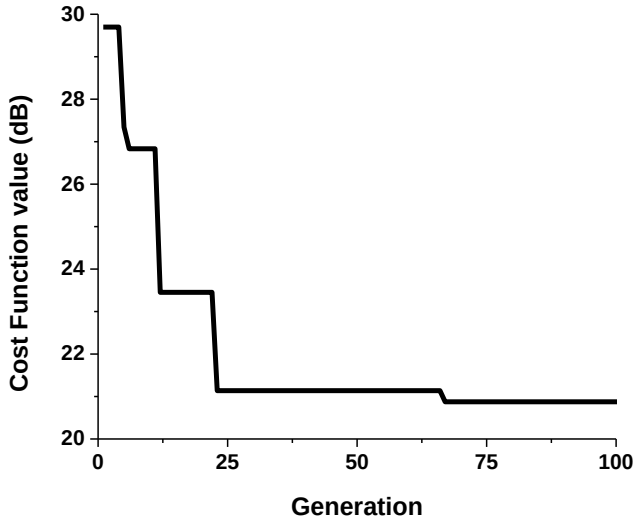

Figure 36. Fitness level of the GA optimizer run for the proposed antenna.

4.3 Detailed Structure of the Proposed Antenna

The final antenna design is proposed in Figure 37 after further modification and analysis to lower the *kr* and improve the CBW. First, the four corners of the antenna substrate are removed to minimize the *kr*. The removal depth (*h*) is chosen to minimize *kr* as larger values increase the lowest frequency of the CBW and smaller values increase the radius of the sphere enclosing the antenna, both of which increase the *kr*. The front side of the antenna, Figure 37(a), consists of the horizontal corner truncated wide slot with meander tips, hexagonal shaped center parasitic patch, and diagonal notches on the four removed vertices of the

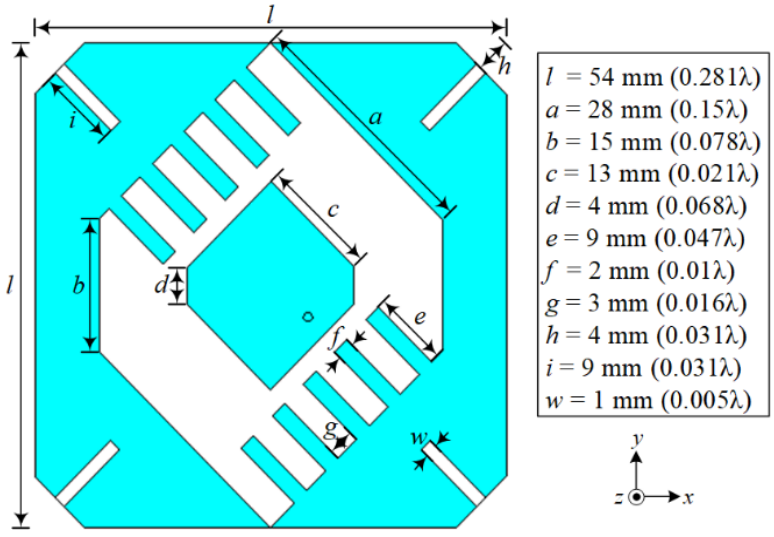

(a)

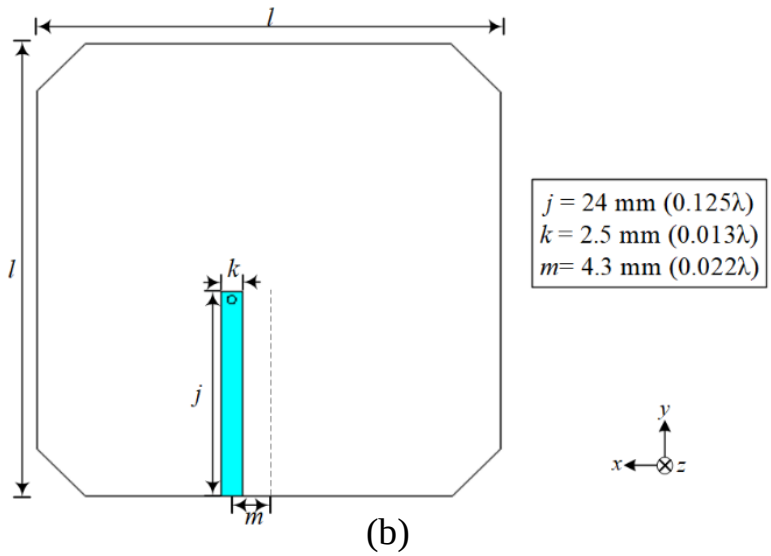

Figure 37. The proposed antenna design and dimensions. (a) Frontside and (b) backside.

antenna. Long side length (*a*) and short side length (*b*) of the wide slot and the patch's long (*c*) and short (*d*) side lengths are selected to generate the widest CBW as different values create discontinuities in the ARBW. Similarly, the length (*i*) and width (*w*) of the rectangular, diagonal notches on the four corners of the antenna are picked to prevent peaks in the ARBW that jump above 3-dB. The dimensions (*e*, *f*, and *g*) of the ten meander tips increase the electrical length and subsequently lower the *kr* while maintaining a broad IBW. The number of meander tips are varied to find the proper value that provides the largest CBW. While using less than ten meander tips, the axial ratio briefly rises above 3-dB reducing the 3-dB ARBW. Also, increasing the number of meander tips beyond ten produce nearly the same –10-dB IBW. However, the lower bound of the axial ratio is shifted upwards increasing the *kr*.

On the backside of the antenna, as depicted in Figure 37(b), the offset feedline is printed with a shorting pin connecting it to the frontside. Feedline length (*j*), width (*k*), and offset (*m*) in conjunction with the shorting pin are chosen for matching. Although the feedline width should be set at 3 mm for proper matching with 50-Ω characteristic impedance [57], the shorting pin provides matching to 50-Ω between the lowest and highest frequency bands to create one large –10-dB IBW. These simulated dimensions give the proposed antenna a *kr* of 1.31 and the overall volume of the antenna is $0.33\lambda \times 0.33\lambda \times 0.008\lambda$, (54 × 54 ×

1.6 mm^3) where λ is calculated at 1.83 GHz, the lowest simulated frequency of the CBW, which will be discussed in section 2.5.

The surface current at the lowest (1.83 GHz) and highest frequency (3.79 GHz) of the simulated CBW are presented in Figure 38 to analyze the CP operation of the designed antenna. At both frequency bounds the surface current is strong along the feedline, so it is hidden to show the surface current on the hexagonal patch and hexagonal slot clearly, from the frontside. The strong currents are circled with accompanying arrows to show the direction of the current, while transparent, red, small circles are shown at the nulls at 70º. The nulls lie where the currents come together or disperse to cancel each other out. The phase starts at 70° and is increased by 90° intervals. At the lowest frequency, Figure 38(a), from 160° to 250°, the location of the strong current moves from the left and right to the bottom and top of the antenna. The same movement of strong current is observed from 250° to 340° from top and bottom to left and right, as well as from 340° to 70° from left and right to bottom and top. Finally, the strong current moves from top and bottom to left and right from 70° to 160°. Following the direction of the strong current this is a counterclockwise (CCW) rotation, which states the antenna propagates RHCP in the +*z* direction. It is shown that at the highest frequency, Figure 38(b), there is an increase in number of strong currents and nulls, which coincides with

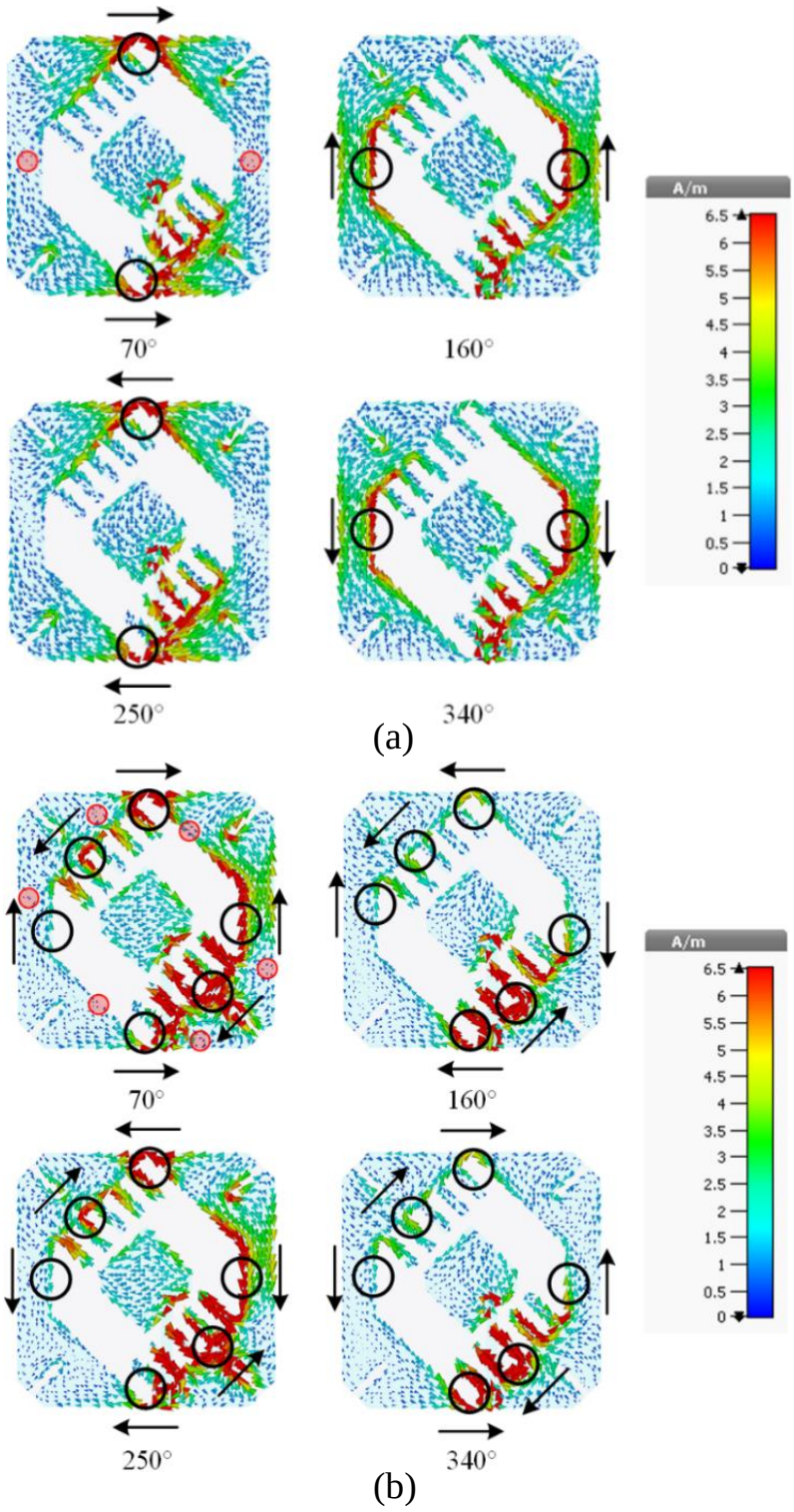

Figure 38. The surface current distribution at (a) 1.83 GHz and (b) 3.79 GHz.

the harmonics of the antenna. An asymmetrical current distribution is observed at the highest frequency. At 70° and 250°, the magnitude of strong current on the left and right sides of the antenna are not equal. The

same imbalance of strong current magnitude can be seen at the top and bottom of the antenna, for 160° and 340°. This inequality of magnitude causes a slightly tilted realized gain pattern at the high end of the CBW, which will be discussed later in section 2.5.

4.4 Results and Discussion

The proposed antenna is then fabricated, shown in Figure 39, to compare the simulation with measured results. The prototype is measured using an Agilent E5063 network analyzer in an anechoic chamber. The simulated and measured S11 and axial ratio (in the +z direction) of the proposed antenna are shown in Figure 40(a) and Figure 40(b), respectively. From simulation, a CBW from 1.83–3.79 GHz or 69.8% (–10-dB IBW of 87.6% [1.59–4.07 GHz] and 3-dB ARBW of 69.8% [1.83–3.79 GHz]) is achieved. Since the forward and backward axial ratio are similar with each other, the axial ratio is only discussed in the forward direction for brevity. The simulated 3-dB axial ratio beamwidths in the front propagation direction for the XZ and YZ plane (back propagation direction for the XZ and YZ plane) at 2.29 GHz are 56.3º and 72.5º (65.2º and 94.1º), at 2.78 GHz are 43.5º and 30.7º (35.9º and 33.9º), and at 3.27 GHz are 32.3º and 24º (29.3º and 22º). Measurements show a CBW from 1.80–3.76 GHz or 70.5% (–10-dB IBW of 89.7% [1.60–4.20 GHz] and 3-dB ARBW of 70.5% [1.80–3.76 GHz]). Both measured S11 and axial ratio match well with the simulated results with minimal discrepancies. A minor frequency shift can be seen in the measured S11 compared to the simulated results, which is likely attributed to fabrication errors including addition of the SMA connector.

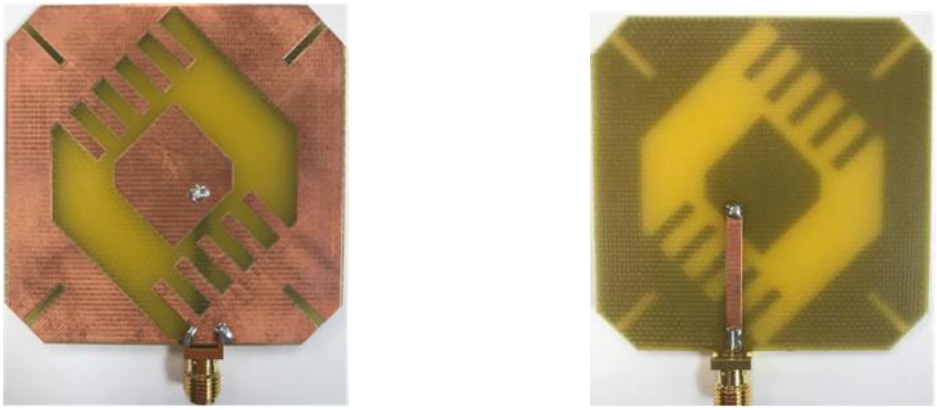

(a) (b)

Figure 39. The prototype of the proposed antenna. (a) Frontside and (b) backside.

Figure 41 shows the simulated and measured forward realized gain vs. frequency of the antenna. The backward realized gain is not presented as it is nearly identical to the forward realized gain in simulation, and the bidirectional capability is discussed with the realized gain pattern. The peak forward realized gain in simulation and measurement are similar at 3.48 and 3.65 dBi, respectively.

Next, simulated and measured realized gain patterns for the 25th (2.29 GHz), 50th (2.78 GHz), and 75th (3.27 GHz) percentile of the measured CBW are presented in Figure 42. Measured results agree well with the simulated results at all three frequencies in both XZ and YZ planes. The antenna propagates nearly equal magnitude in the +z direction and the -z direction which proves the bidirectional capabilities of the proposed antenna. At the 75th percentile, the pattern becomes slightly tilted which is attributed to the less symmetrical surface current at the high end of the frequency band. The realized gain pattern at the 75th percentile is still bidirectional, with a 1.8 dBi magnitude at 0º and a 1.5 dBi magnitude at 180º which is only a 1 dBi difference when compared to the realized gain magnitude at the 25th percentile 0º. A tilted radiation pattern at higher frequencies is a common issue amongst broadband CP antennas [23, 27, 29].

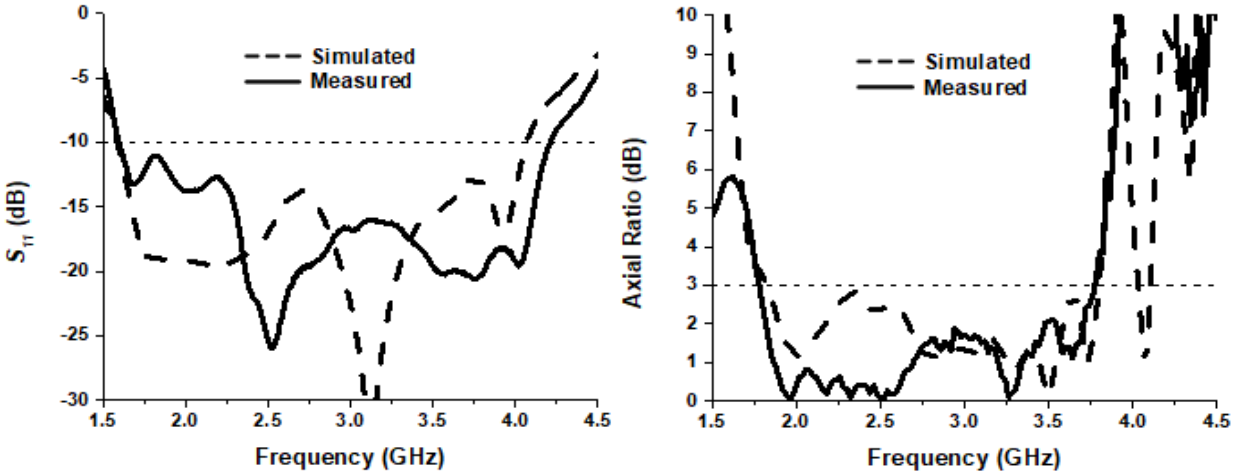

(a) (b)

Figure 40. The simulated and measured (a) S_{11} and (b) axial ratio.

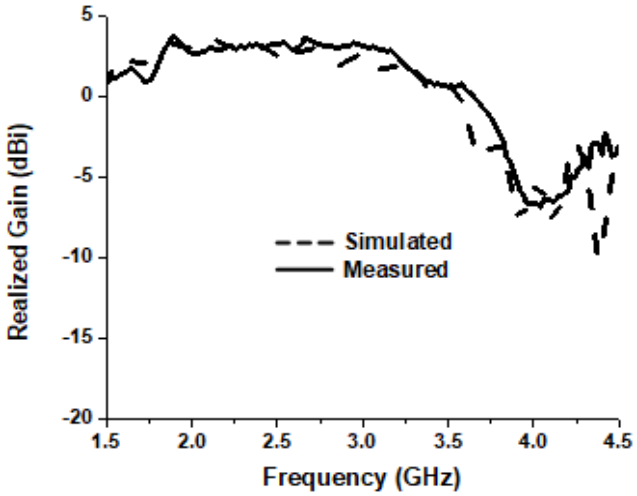

Figure 41. The simulated and measured realized gain (in +*z* direction) vs. frequency of the proposed antenna.

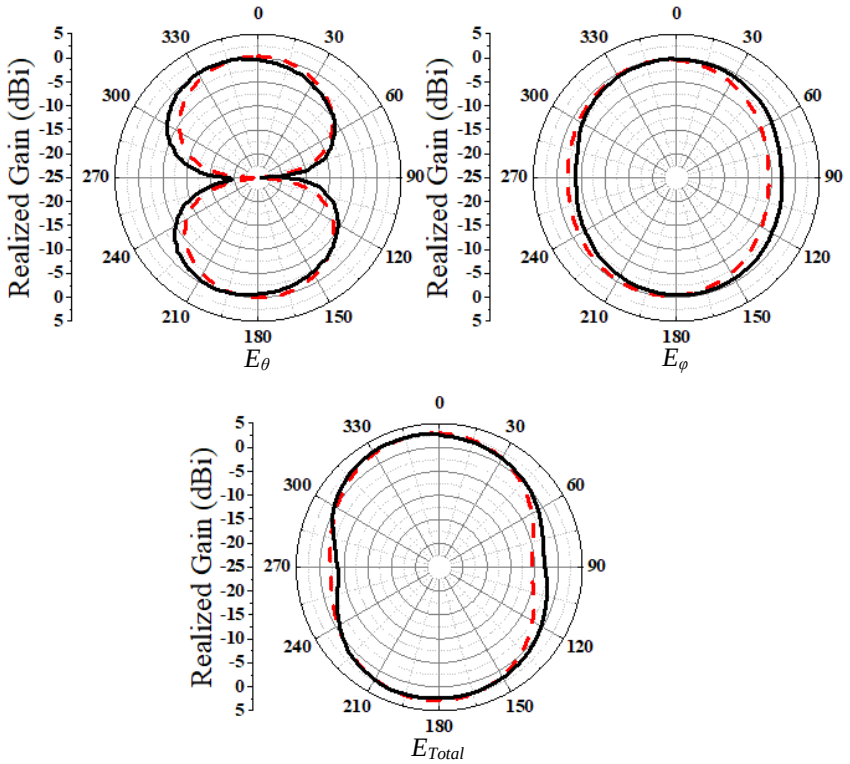

(a)

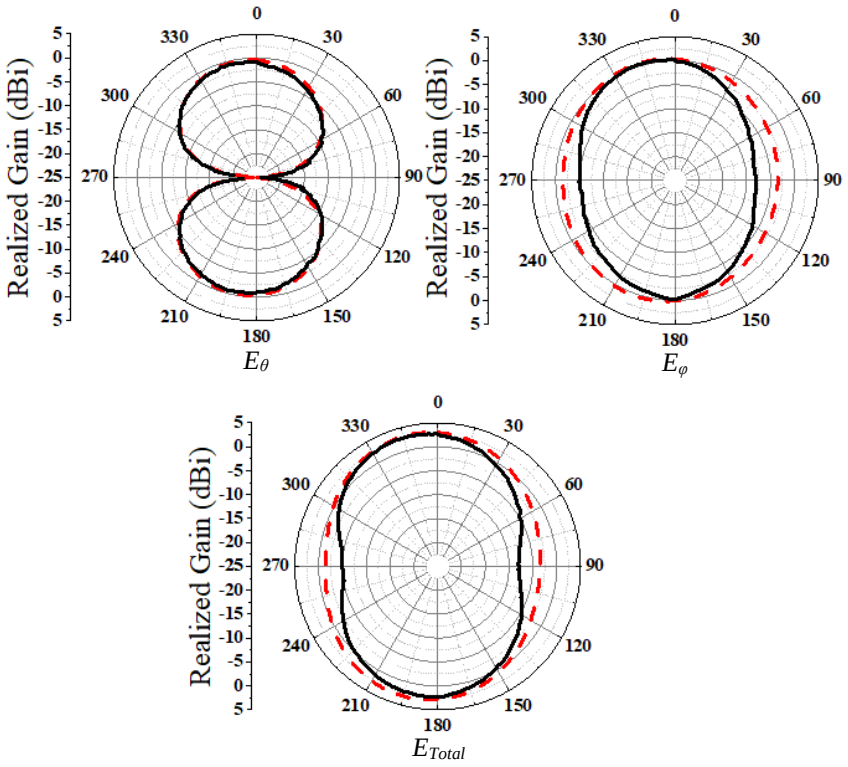
Realized Gain (dBi)
E_θ
E_φ
E_{Total}

(b)

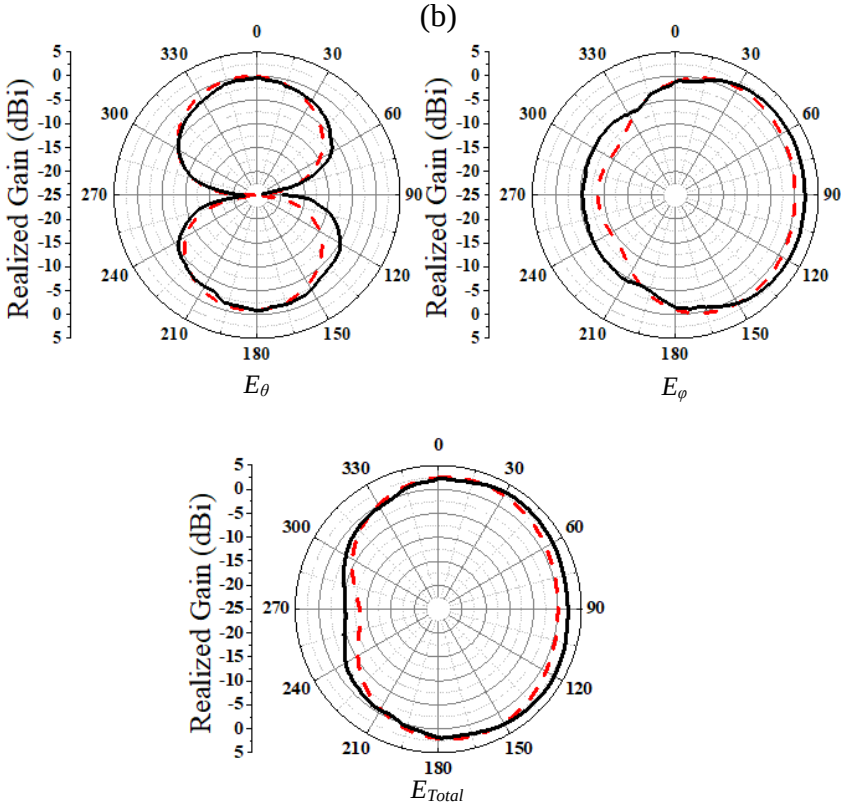
Realized Gain (dBi)
E_θ
E_φ
E_{Total}

(c)

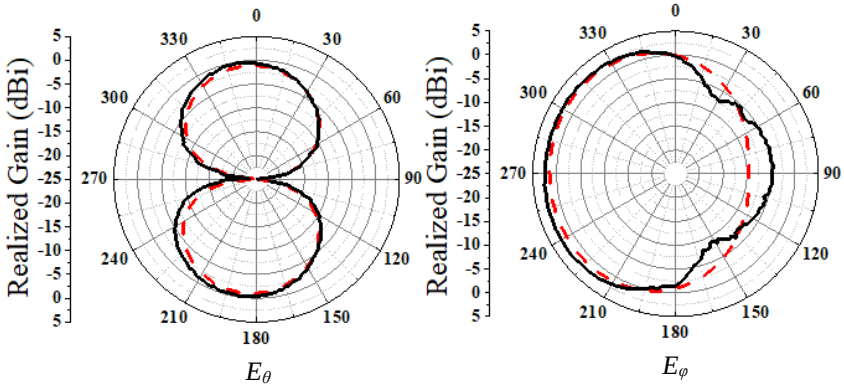
Realized Gain (dBi)
E_θ
E_φ

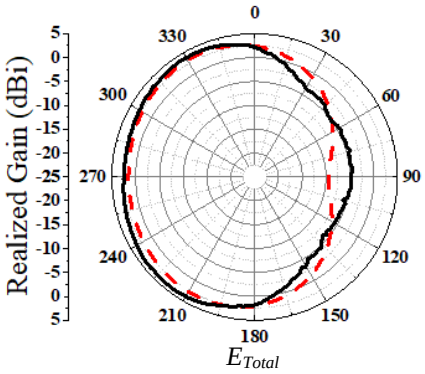
Realized Gain (dBi)
E_{Total}

(d)

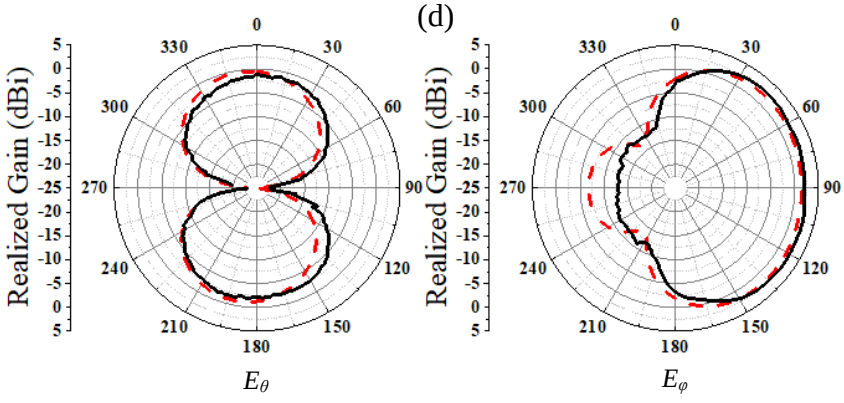
Realized Gain (dBi)
E_θ
E_φ

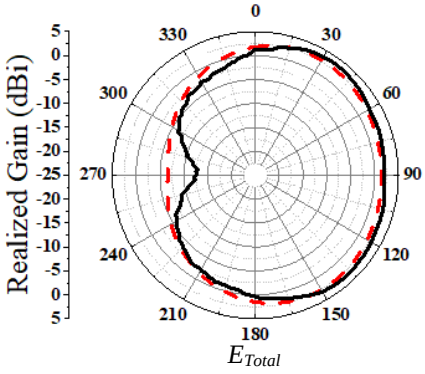
Realized Gain (dBi)
E_{Total}

(e)

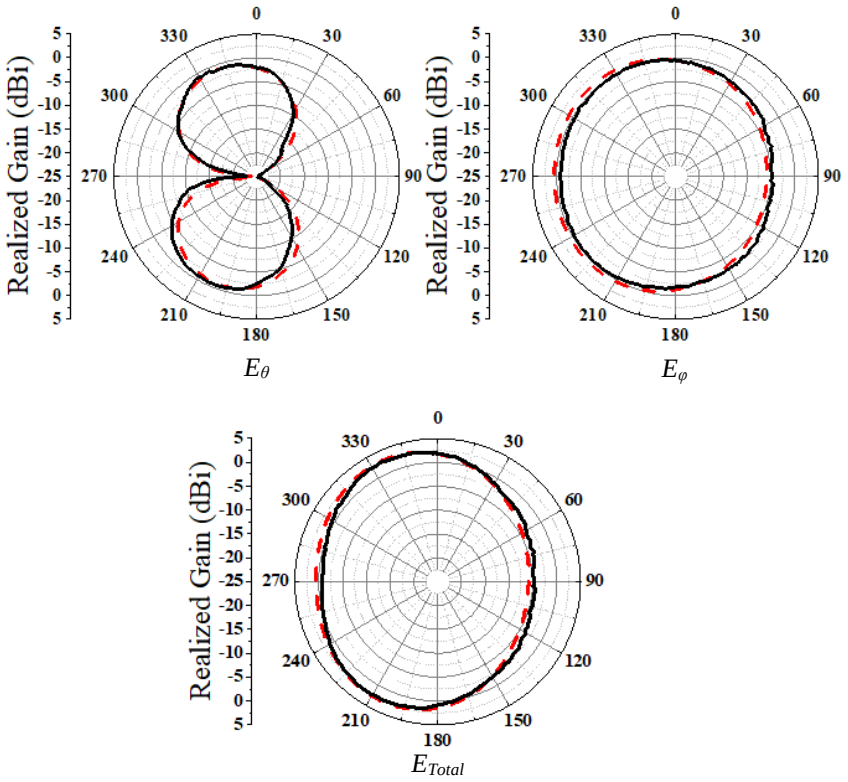

(f)

Figure 42. Realized gain patterns at 2.29 GHz in (a) XZ plane (b) YZ plane, at 2.78 GHz in (c) XZ plane (d) YZ plane, and at 3.27 GHz in (e) XZ plane (f) YZ plane.

4.5 Conclusion

A size-reduced, broadband, CP antenna printed on FR4 substrate is proposed to achieve bidirectionality. A prototype of the antenna is constructed and measured to verify results obtained from simulation. The electrical size of the antenna is a *kr* of 1.31. The measured results show a CBW of 70.5% from 1.80–3.76 GHz, with minimal differences from the simulated antenna. The proposed antenna has a peak forward realized gain of 3.65 dBi at 1.88 GHz. The backward realized gain is similar to the forward realized gain. Due to its reduced size, broad CBW, CP, and bidirectional radiation pattern this antenna is suitable for multiple wireless communication frequency bands in long and narrow application scenarios.

CHAPTER 5

CONCLUSION

In this thesis three bidirectional antennas are designed and discussed for applications in bidirectional scenarios with miniaturization. Circular polarization is achieved in the antenna designs as communication systems benefit for circular polarization through the reduction of multipath interference and polarization mismatch.

Chapter 1 introduces antenna characteristics such as S_{11}, directivity, gain, realized gain, and axial ratio. Yagi antennas are shown as a common method to provide high directivity with a simple antenna design. Both top loading and close spacing are presented as techniques to reduce the size of antennas, as well as methods to counteract the harmful radiation resistance drop that is noted at small electrical sizes. Planar antennas are discussed as modern applications admire their low cost and conformal structures. The method of antenna measurement is explained using a network analyzer to gather data for the resulting calculations.

Chapter 2 shows the design of a pattern reconfigurable, circularly polarized, parasitic array with two unidirectional states to allow for bidirectional propagation with high realized gain. Two switch circuits are constructed in the center of the two director elements that operate using PIN diodes. The configuration of the circuit allows a single 1.5 V button cell battery to control the propagation direction by turning on the correct director element. The 0.02λ inner element spacing as well as the top loading allows the entire array to have a 0.78 kr.

Chapter 3 provides the analysis of a printed, bidirectional, circularly polarized cross dipole with an electrically small size. Arced top loading on the ends of the dipole arms, as well as utilizing both sides of the substrate allow the antenna to achieve a 0.65 kr. Since the electrical size is smaller than 0.8, the radiation resistance is diminished providing poor matching to characteristic impedance. To boost the reduced resistance, a square t-matching stub is used to connect the dipole arms on each side.

Chapter 4 presents a broadband, planar, circularly polarized, bidirectional antenna. Utilization of meander tips and the rotation of the slot and parasitic patch allow for a broad impedance bandwidth. Size reduction is achieved using meander tips on the rotated slot and inserting a parasitic patch to extend the

electrical length thus shifting the resonant frequency lower. The total size of the optimized antenna is 54 × 54 × 1.6 mm^3 and the design is printed on FR4 substrate with promising measured results of a 89.7% -10-dB IBW, a 70.5% 3-dB ARBW, and a peak realized gain of 3.65 dBi.

Future work will be to modify the two-sided, cross dipole antenna for sense reconfiguration. In the same manner that the work in Chapter 2 implements PIN diodes, the diodes can be used to turn on/off select parts of the cross dipole to change the sense between four states: RHCP, LHCP, Vertical LP, and Horizontal LP. After further design changes to chapter 3 and improvements to the bandwidth in chapter 2, the works presented in this thesis will be submitted to a peer review journal for publication.

REFERENCES

1. W. H. Hayt, Jr. and J. A. Buck, Engineering Electromagnetics, 8th ed. New York: McGraw-Hill, 2010.
2. C. A. Balanis, Antenna Theory Analysis and Design, Hoboken: Wiley & Sons, 2005.
3. M. F. Bolster, "A new type of circular polarizer using crossed dipoles," IRE Trans. Microw. Theory Tech., vol. 9, no. 9, pp. 385–388, Sep. 1961.
4. P. P. Viezbicke, "Yagi Antenna Design." NBS Technical Note 688, 1976.
5. D. F. Sievenpiper, et al. "Experimental validation of performance limits and design guidelines for small antennas," *IEEE Transactions on Antennas and Propagation*, 2012: 8-19.
6. S. Lim, J. Chen, and C. Cato, "Design of a thin, electrically small, two-element parasitic array with circular polarization," IEEE Antennas Wireless Propag. Lett., vol. 17, no. 6, pp. 1006–1009, June 2018.
7. J. J. Yu and S. Lim, "Design of an electrically small, circularly polarized, parasitic array antenna for an active 433.92-MHz RFID handheld reader," IEEE Trans. Antennas Propag., vol. 60, no. 5, pp. 2549–2554, May 2012.
8. S. S. Gao, Q. Luo, and F. Zhu, Circularly Polarized Antennas. Hoboken, NJ, USA: Wiley, 2014.
9. B. Y. Toh, R. Cahill, and V. F. Fusco, "Understanding and measuring circular polarization," IEEE Transactions on Education, vol. 46, no. 3, pp. 313-318, Aug. 2003.
10. L. P. Smith, J. C. Howell, and S. Lim, "A size-reduced, 15-element, planar yagi antenna," in IEEE Trans. Antennas Propag., vol. 69, no. 4, pp. 2410-2415, Apr. 2021.
11. J. Chen, J. Ludwig, and S. Lim, "Design of a compact log-periodic dipole array using t-shaped top loadings," IEEE Antennas Wireless Propag. Lett., vol. 16, pp. 1585-1588, 2017.
12. S. Lim and H. Ling, "Design of a closely spaced, folded yagi antenna," IEEE Antennas Wireless Propag. Lett., vol. 5, 2006.
13. C. M. Kruesi, R. J. Vyas, and M. M. Tentzeris, "Design and development of a novel 3-D cubic antenna for wireless sensor networks (WSNs) and RFID applications," IEEE Trans. Antennas Propag., vol. 57, no. 10, pp. 3293-3299, Dec. 2009.

14. H. K. Ryu, G. Jung, D. K. Ju, S. Lim, and J. M. Woo, "An electrically small spherical UHF RFID tag antenna with quasi-isotropic patterns for wireless sensor networks," IEEE Antennas Wireless Propag. Lett., vol. 9, pp. 60-62, 2010.
15. S. Lim and H. Ling, "Design of electrically small, pattern reconfigurable yagi antenna," IET Electron. Lett., vol. 43, no. 24, Nov. 2007.
16. H. Wheeler, "Fundamental limitations of small antennas," Proceedings of the IRE, vol. 35, no. 12, pp. 1479-1494, 1947.
17. L. J. Chu, "Physical limitations of omni-directional antennas," Journal of Applied Physics, pp. 1163-1175, 1948.
18. K. Sarabandi and R. Azadegan, "Design of an efficient miniaturized UHF planar antenna," IEEE Trans. Antennas Propag., vol. 51, no. 6, pp. 1270–1276, Jun. 2003.
19. H.-K. Ryu, J.-M. Woo, "Miniaturisation of rectangular loop antenna using meander line for RFID tags," IET Electron. Lett., vol. 43, no. 7, pp. 372-374, Mar. 2007.
20. P. Jin and R. Ziolkowski, "Metamaterial-inspired, electrically small Huygens source," *IEEE Antennas Wireless Propag. Lett.*, vol. 9, pp. 501-505, 2010.
21. R. Ziolkowski, "Low profile, broadside radiating, electrically small Huygens source antennas," *IEEE Access*, vol. 3, pp. 2644-2651, Dec. 2015.
22. J. Oh and K. Sarabandi, "Low profile vertically polarized omnidirectional wideband antenna with capacitively coupled parasitic elements," *IEEE Trans. Antennas Propag.*, vol. 62, no. 2, pp. 977-982, Feb. 2014.
23. P. Jin, C. Lin, and R. Ziolkowski, "Multifunctional, electrically small, planar near-field resonant parasitic antennas," *IEEE Antennas Wireless Propag. Lett.,* vol. 11, pp. 200–204, 2012.
24. M. Tang, T. Shi, and R. Ziolkowski, "A study of 28 GHz, planar, multilayered, electrically small, broadside radiating, Huygens source antennas," *IEEE Trans. Antennas Propag.,* vol. 65, no. 12, pp. 6345–6354, Dec. 2017.

25. W. Lin and R. Ziolkowski, “Electrically small, low-profile, Huygens circularly polarized antenna,” *IEEE Trans. Antennas Propag.*, vol. 66, no. 2, pp. 636–643, Feb. 2018.
26. H. Bagheroghli, “A novel circularly polarized microstrip antenna with two connected quasi monopoles for wideband applications,” *IEEE Antennas Wireless Propag. Lett.*, vol. 12, pp. 1343-1346, Oct. 2013.
27. K. O. Gyasi, et al., “A compact broadband cross-shaped circularly polarized planar monopole antenna with a ground plane extension,” *IEEE Antennas Wireless Propag. Lett.*, vol. 17, no. 2, pp. 335-338, Feb. 2018.
28. Z. Wu, M.-C. Tang, M. Li, and R. Ziolkowski, “Ultalow-profile, electrically small, pattern-reconfigurable metamaterial-inspired Huygens dipole antenna,” *IEEE Trans. Antennas Propag.*, vol. 68, no. 3, pp. 1238-1248, Mar. 2020.
29. A. Narbudowicz, S. Chalermwisutkul, P. J. Soh, M. F. Jamlos, and M. J. Ammann, “Compact UHF antenna utilizing CubeSat’s characteristic modes,” *EuCAP*, Krakow, Poland, pp. 1-3, 2019.
30. H. H. Tran, S. X. Ta, and I. Park, “A compact circularly polarized crossed-dipole antenna for an RFID tag,” IEEE Antennas Wireless Propag. Lett., vol. 14, pp. 674–677, Dec. 2014.
31. S. X. Ta, I. Park, and R. W. Ziolkowski, “Crossed dipole antennas: a review.,” IEEE Antennas Propag. Magazine, vol. 57, no. 5, pp. 107–122, Oct. 2015.
32. Y. Zhang and T. Fukusako, “Design of circularly polarized low-profile and slender antenna with a helical element,” IEEE Antennas Wireless Propag. Lett., vol. 11, pp. 523–526, May 2012.
33. Y. Shi and J. Liu, “A circularly polarized octagon-star-shaped microstrip patch antenna with conical radiation pattern,” IEEE Trans. Antennas Propag., vol. 66, no. 4, Apr. 2018.
34. S. X. Ta and I. Park, “Crossed dipole loaded with magneto-electric dipole for wideband and wide-beam circularly polarized radiation,” IEEE Antennas Wireless Propag. Lett., vol. 14, pp. 358–361, Oct. 2014.
35. W. Yang, Y. Pan, S. Zheng, and P. Hu, “A low-profile wideband circularly polarized crossed-dipole antenna,” IEEE Antennas Wireless Propag. Lett., vol. 16, pp. 2126–2129, May 2017.
36. Y.-X. Guo and D. C. H. Tan, “Wideband single-feed circularly polarized patch antenna with conical radiation pattern,” IEEE Antennas Wireless Propag. Lett., vol. 8, pp. 924–926, July 2009.
37. C. Sun, Z. Wu, and B. Bai, “A novel compact wideband patch antenna for GNSS application,” IEEE Trans.

Antennas Propag., vol. 65, no. 12, pp. 7334–7339, Dec. 2017.

38. J. Chatterjee, A. Mohan, and V. Dixit, “Broadband circularly polarized H-shaped patch antenna using reactive impedance surface,” IEEE Antennas Wireless Propag. Lett., vol. 17, no. 4, pp. 625–628, Apr. 2018.
39. K. Y. Lam, K.-M. Luk, K. F. Lee, H. Wong, and K. B. Ng, “Small circularly polarized u-slot wideband patch antenna,” IEEE Antennas Wireless Propag. Lett., vol. 10, pp. 87–90, Feb. 2011.
40. H. Zhang, Y. Guo, and G. Wang, “A wideband circularly polarized crossed-slot antenna with stable phase center,” IEEE Antennas Wireless Propag. Lett., vol. 18, no. 5, pp. 941–945, May 2019.
41. J.-M. Chen and J.-S. Row, “Wideband circularly polarized slotted-patch antenna with a reflector,” IEEE Antennas Wireless Propag. Lett., vol. 14, pp. 575–578, Nov. 2014.
42. J. Wei, X. Jiang, and L. Peng, “Ultrawideband and high-gain circularly polarized antenna with double-y-shape slot,” IEEE Antennas Wireless Propag. Lett., vol. 16, pp. 1508–1511, Jan. 2017.
43. L. Lu, Y.-C. Jiao, H. Zhang, R. Wang, and T. Li, “Wideband circularly polarized antenna with stair-shaped dielectric resonator and open-ended slot ground,” IEEE Antennas Wireless Propag. Lett., vol. 15, pp. 1755-1758, Feb. 2016.
44. J.-Y. Jan, C.-Y. Pan, K.-Y. Chiu, and H.-M. Chen, “Broadband CPW-fed circularly-polarized slot antenna with an open slot,” IEEE Trans. Antennas Propag., vol. 61, no. 3, pp. 1418–1422, Mar. 2013.
45. H. Bagheroghli, “A novel circularly polarized microstrip antenna with two connected quasi monopoles for wideband applications,” IEEE Antennas Wireless Propag. Lett., vol. 12, pp. 1343–1346, Oct. 2013.
46. R. K. Saini, S. Dwari, and M. K. Mandal, “CPW-fed dual-band dual-sense circularly polarized monopole antenna,” IEEE Antennas Wireless Propag. Lett., vol. 16, pp. 2497–2500, July 2017.
47. K. O. Gyasi, et al., “A compact broadband cross-shaped circularly polarized planar monopole antenna with a ground plane extension,” IEEE Antennas Wireless Propag. Lett., vol. 17, no. 2, pp. 335–338, Feb. 2018.
48. C. F. Zhou and S. W. Cheung, “A wideband CP crossed slot antenna using 1-λ resonant mode with single feeding,” IEEE Trans. Antennas Propag., vol. 65, no. 8, Aug. 2017.
49. U. Ullah and S. Koziel, “A broadband circularly polarized wide-slot antenna with a miniaturized footprint,” IEEE Antennas Wireless Propag. Lett., vol. 17, no. 12, pp. 2454–2458, Dec. 2018.

50. M. S. Ellis, Z. Zhao, J. Wu, X. Ding, Z. Nie, and Q.-H. Liu, “A novel simple and compact microstrip-fed circularly polarized wide slot antenna with wide axial ratio bandwidth for C-band applications,” IEEE Trans. Antennas Propag., vol. 64, no. 4, pp. 1552–1555, Apr. 2016.
51. M. Nosrati and N. Tavassolian, “Miniaturized circularly polarized square slot antenna with enhanced axial-ratio bandwidth using an antipodal Y-strip,” IEEE Antennas Wireless Propag. Lett., vol. 16, pp. 817–820, Sep. 2016.
52. Y. Ojaroudi, N. Ojaroudi, and N. Ghadimi, “Circularly polarized microstrip slot antenna with a pair of spur-shaped slits for WLAN applications,” Microw. Opt. Technol. Lett., vol. 57, no. 3, pp. 756–759, Mar. 2015.
53. J. Shen, C. Lu, W. Cao, J. Yang, and M. Li, “A novel bidirectional antenna with broadband circularly polarized radiation in X-band,” IEEE Antennas Wireless Propag. Lett., vol. 13, pp. 7–10, Dec. 2013.
54. J.-Y. Jan and J.-W. Su, “Bandwidth enhancement of a printed wide-slot antenna with a rotated slot,” IEEE Trans. Antennas Propag., vol. 53, no. 6, pp. 2111–2114, June 2005.
55. Y. Sung, “Bandwidth enhancement of a microstrip line-fed printed wide- slot antenna with a parasitic center patch,” IEEE Trans. Antennas Propag., vol. 60, no. 4, pp. 1712–1716, Apr. 2012.
56. X. Zhang and L. Zhu, “Patch antennas with loading of a pair of shorting pins toward flexible impedance matching and low cross polarization,” IEEE Trans. Antennas Propag. vol. 64, no. 4, Apr. 2016.
57. D. M. Pozar, Microwave Engineering, 4th ed. New York: Wiley, 2011.